Rock Mechanics and Rock Engineering (2019) 52:517–542
https://doi.org/10.1007/s00603-018-1597-8

ORIGINAL PAPER

Stress Measurements for an In Situ Stimulation Experiment in Crystalline Rock: Integration of Induced Seismicity, Stress Relief and Hydraulic Methods

Hannes Krietsch[1] · Valentin Gischig[1] · Keith Evans[1] · Joseph Doetsch[1] · Nathan Oliver Dutler[2] · Benoît Valley[2] · Florian Amann[3]

Received: 25 January 2018 / Accepted: 16 September 2018 / Published online: 27 September 2018

Abstract
An extensive campaign to characterize rock stresses on the decameter scale was carried out in three 18–24 m long boreholes drilled from a tunnel in foliated granite at the Grimsel Test Site, Switzerland. The survey combined stress relief methods with hydrofracturing (HF) tests and concomitant monitoring of induced seismicity. Hydrofracture traces at the borehole wall were visualized with impression packer tests. The microseismic clouds indicate sub-vertical south-dipping HFs. Initial inversion of the overcoring strains with an isotropic rock model yielded stress tensors that disagreed with the HF and microseismic results. The discrepancy was eliminated using a transversely isotropic rock model, parametrized by a novel method that used numerical modelling of the in situ biaxial cell data to determine the requisite five independent elastic parameters. The results show that stress is reasonably uniform in the rock volume that lies to the south of a shear zone that cuts the NNW of the study volume. Stress in this volume is considered to be unperturbed by structures, and has principal stress magnitudes of 13.1–14.4 MPa for σ_1, 9.2–10.2 MPa for σ_2, and 8.6–9.7 MPa for σ_3 with σ_1 plunging to the east at 30–40°. To the NNW of the uniform stress regime, the minimum principal stress declines and the principal axes rotate as the shear zone is approached. The stress perturbation is clearly associated with the shear zone, and may reflect the presence of more fragmented rock acting as a compliant inclusion, or remnant stresses arising from slip on the shear zone in the past.

Keywords Overcoring · Hydraulic fracturing · Integration of stress relief and hydraulic methods · Transversely isotropic media · Stress inversion

1 Introduction

Knowledge of the in situ stress field is crucial for many geotechnical applications and rock mechanical problems (e.g., tunneling, mining, hydropower, nuclear waste storage, EGS), (see Bjarnason et al. 1988; Christiansson and Janson 2003, Ask 2006a). There is a broad range of methods used to measure in situ stress, all of which have advantages and disadvantages with respect to measurement reliability, spatial resolution and coverage as well as to which components of the

✉ Hannes Krietsch
hannes.krietsch@erdw.ethz.ch

Valentin Gischig
gischig@erdw.ethz.ch

Keith Evans
Keith.evans@erdw.ethz.ch

Joseph Doetsch
Joseph.doetsch@erdw.ethz.ch

Nathan Oliver Dutler
nathan.dutler@unine.ch

Benoît Valley
benoit.valley@unine.ch

Florian Amann
amann@lih.rwth-aachen.de

[1] Department of Earth Sciences, ETH Zurich, Sonneggstrasse 5, 8092 Zurich, Switzerland

[2] Center for Hydrogeology and Geothermics (CHYN), University of Neuchâtel, Rue Emile Argand 11, 2000 Neuchâtel, Switzerland

[3] Chair of Engineering Geology and Environmental Management, RWTH Aachen, Lochnerstrasse 4-20, 52064 Aachen, Germany

stress tensor are resolved (Amadei and Stephansson 1997). The stress measurement techniques can be classified into two general categories: (1) measurements based on the elastic response of rocks and (2) measurements based on the failure of rocks. In this paper, we compare and combine the results from overcoring measurements (stress relief technique), which falls in the first category above, and the hydraulic fracturing and HTPF (hydraulic testing on pre-existing fractures) techniques, which fall in the second category above. Overcoring is applied in short boreholes (i.e., a few tens of meters long) and may provide an estimate of several or all components of the stress tensor depending on what deformation components are measured by the overcored probe. During overcoring, the relaxation strains of the overcored specimen are recorded and inverted for the in situ stresses using Hooke's law (Amadei and Stephansson 1997), assuming that the rock remains in its elastic domain. The required elastic parameters are usually obtained from biaxial tests that are conducted on-site immediately after overcoring. Derivation of the elastic properties from biaxial tests and the subsequent inversion of the overcoring strains to estimate the stresses is often based on the assumption of an isotropic linear elastic constitutive behavior (e.g., Bjarnason et al. 1988; Leijon 1989, Ask 2003, 2006b; Christiansson and Janson 2003). However, solutions for the inversion of overcoring strains are available for transversely isotropic rock (Amadei 1996), although the estimation of the five independent elastic parameters needed for the inversion requires the biaxial test data be modelled with additional constraints from other tests (Sjöberg et al. 2003). Hydraulic methods give direct estimates of the normal stresses acting on induced (in case of HF) or pre-existing (in case of HTPF) fractures. HF usually provides an estimate of the magnitude of σ_3, because the initiated fracture usually propagates in the plane normal to σ_3. However, caution is necessary for tests conducted in anisotropic rock that has a plane of mechanical weakness as the fracture may initiate and propagate some distance within that plane (Gischig et al. 2018). HTPF measurements on an arbitrarily oriented pre-existing fracture provide an estimate of the normal stress acting on the fracture, which may not coincide with a principal stress direction. A minimum of six sets of measurements on fractures in different orientations are needed to solve the principal stress magnitudes and orientations.

Generally, a smaller rock volume than the actual volume of interest is probed during single in situ stress measurements because of the pointwise measurement character of these methods (Ask 2006b). For instance, the rock volume of influence ranges from 10^{-3} to 10^{-2} m^3 for overcoring, over 1–10 m^3 for hydraulic testing of pre-existing fractures, to 0.5–50 m^3 for hydraulic fracturing (Amadei and Stephansson 1997). As the rock volume of interest is typically larger than that of a single measurement, and the latter may not be representative of the larger volume owing to stress heterogeneity, many measurements are required across the target rock mass to characterize the stress state and its heterogeneities. Multiple measurements also allow an assessment of the consistency of the measurements and the identification and mitigation of potential measurements inaccuracies, thereby helping to build confidence in the stress estimation. Three different spatial scales can be distinguished: (a) the test scale of a single measurement, (b) the measuring location scale that includes all measurements, and (c) the scale of the rock engineering problem (Leijon 1989). An overall tensor for the rock engineering scale can be obtained by integrating the different data. The different physical nature of each method, the scale, available data, and thus the potentially different stress results require great care in their integration and interpretation (Ask 2006a).

Besides the average stress field on the scale of interest, it is also important to consider stress heterogeneities, such as might result from material property contrasts (e.g., a change in lithology or degree of fragmentation that produces stiffness contrasts), large fault zones, and past slip along faults. Thus, detailed stress characterization should not aim only at a representative mean stress tensor, but also its spatial variations within the rock mass. The integration of various stress measurements within a heterogeneous rock mass is not straightforward as the linear interpolation of the stress field may be inappropriate (Barton and Zoback 1994). Evans et al. (1989) examined systematic variations in stress magnitude between sandstones and shales in the Appalachian basin and related this to the effect of stiffness variations on tectonic straining. Various authors (Pahl et al. 1989; Bell et al. 1992; Wileveau et al. 2007; Valley and Evans 2009, 2010) described stress heterogeneities in terms of change in magnitudes and rotation of the horizontal stresses, due to faults and fracture zones.

Integration of results from different methods is desirable because most methods by themselves do not constrain all components of the stress tensor, the exception being some overcoring techniques. One such scheme for combining results is the Integrated Stress Determination Method (ISDM) (Cornet 1993, Ask 2006a), which was applied to stress measurements in Äspö, Sweden, and produced reliable estimates of the in situ stress field. However, the approach assumes isotropic rock and cannot account for the effect of anisotropy arising, for example, through pervasive foliation on the stress field. In addition, the data considered in joint inversions needs to be chosen with care, because undetected errors in observations or stress field heterogeneity may compromise the joint stress estimate.

We present here the results of an extensive stress characterization survey that combines hydraulic (HF and HTPF) methods and stress relief methods (i.e., overcoring of CSIRO HI and USBM probes). The stress measurements

were conducted in the framework of a hydraulic stimulation experiment (called the 'In situ Stimulation and Circulation (ISC) Experiment') which was recently conducted at the Grimsel Test Site (owned by Nagra) in central Switzerland (Fig. 1) (Amann et al. 2018). This decameter scale experiment (i.e., test volume 30 m × 30 m × 30 m) addresses open questions concerning induced seismicity, permeability enhancement, and hydromechanical fault response during hydraulic reservoir stimulation in the context of enhanced geothermal systems (EGS). During hydraulic stimulation, fluid is injected into low permeable rock to create new fractures (i.e., hydraulic fracturing) or shear pre-existing fractures (i.e., hydraulic shearing) to enhance permeability of low permeable rock and to create a heat exchanger for sustainable electricity production. The in situ stress field is an important reservoir property affecting its response to hydraulic stimulation.

It is relevant to note that a comparable in situ stimulation experiment was carried out at Äspö HRL in 2015 with the goal of testing the effect of different fluid injection schemes on induced seismicity, as well as evaluating various stimulation monitoring techniques (i.e., acoustic emission, microseismicity and electro-magnetic monitoring).

In this paper, the different stress measurements are analyzed individually and later integrated towards a reliable estimate of the in situ stress tensor relevant for the ISC experiment. Using a sequential integration approach—as opposed to a joint inversion—we identify experimental flaws and demonstrate the importance of considering rock anisotropy in our analysis of both hydrofracture and overcoring data. Furthermore, we present a new method to derive the five independent elastic parameters required for the analysis of overcoring data obtained from tests in the transversely isotropic rock of the ISC site.

1.1 Geological Settings at the Grimsel Test Site (GTS)

The GTS is located at the boundary between the Central Aare Granite and the Grimsel Granodiorite that form the central part of the Aar Massive in the central Swiss Alps (Schneeberger et al. 2017). Both lithologies contain intermediate-grade (greenschist facies) metamorphosed igneous rocks (peak temperature 450 ± 30 °C and peak pressure 600 ± 100 MPa, see Challandes et al. 2008) and appear as relatively undisturbed foliated rock masses (i.e., very few small-scale fractures). These are crosscut by major sub-vertical ductile to brittle-ductile shear zones, as well as EW-striking and south-dipping metabasic dykes. The detailed geological characteristics of the test volume, such as the locations of pre-existing fractures and shear zones, the fracture density distribution, and the orientation of foliation are known from combining geophysical borehole logging (i.e., optical televiewer logging), core logging and tunnel mapping.

The foliation has an average orientation of 140/80° (dip direction/dip), which does not vary significantly in the test volume. The P-wave velocity anisotropy within the test

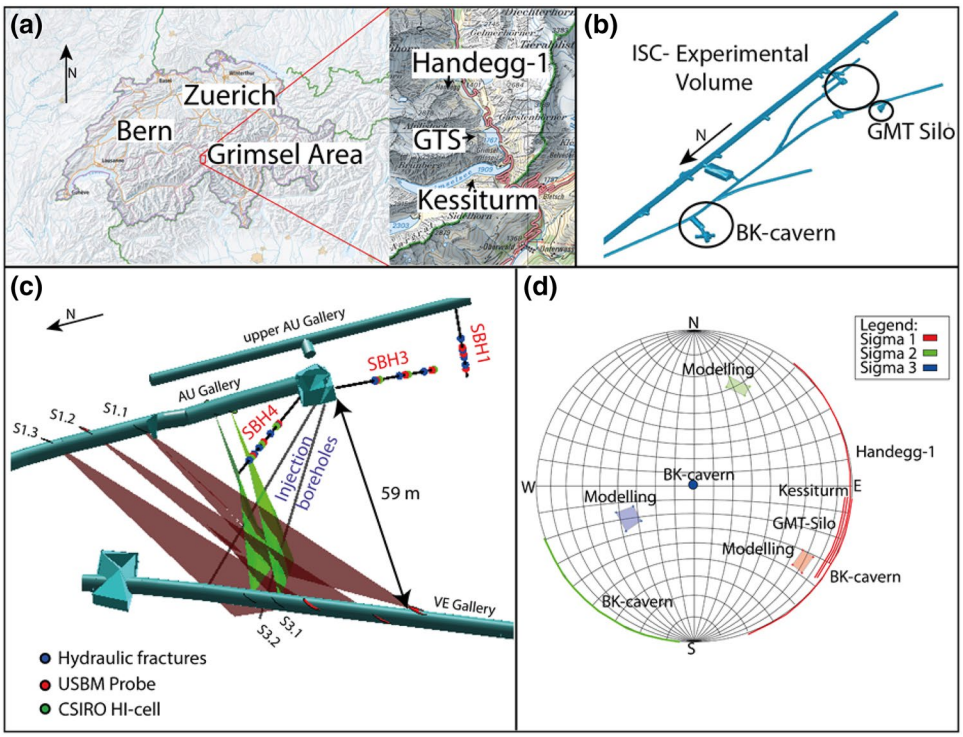

Fig. 1 Location of the Grimsel Test Site and the ISC target volume: **a** map of Switzerland with indicated location of Grimsel Test Site and previous stress measurements outside of GTS (modified from map.geo.admin.ch), **b** sketch of the GTS tunnel system with the ISC experimental volume and two previous stress measurements inside the laboratory, **c** image of the ISC experiment site, including the stress measurement boreholes (SBH1, 3 and 4), the injection boreholes for the ISC experiment, indicated shear zones (red and green planes labelled S1.1–3 and S3.1–2) and the locations of the stress measurements, and **d** results of previously conducted stress measurements. (Color figure online)

volume but away from shear zones is about 7% (Doetsch et al. 2017). Three shear zone directions, denoted as S1, S2 and S3 (Fig. 1), are recognized within the GTS (Steck 1968). (1) The S1 shear zone belongs to the oldest set and follows an orientation of 142/77°. (2) The S2 direction is slightly discordant to S1 with an orientation 157/75°, and is associated with the alpine deformation phase that formed the foliation. The S1 and S2 orientations are hard to distinguish within the ISC test volume so that structures that show one of those orientations will be considered to be S1. (3) The S3 orientation is the youngest of the three and has an orientation of 183/65°. This shear zone contains indicators that suggest a dextral strike slip movement (Keusen et al. 1989; Wehrens et al. 2017).

Within the ISC test volume, the S1 shear zone is characterized by a significantly more distinct foliation compared to the host rock and the presence of brittle fractures in various orientations which are partly filled with gouge. The dominant tectonic feature in the ISC rock volume is a major fault zone that consists of two S3-oriented shear zones associated with two large, biotite-rich metabasic dykes that are up to 1 m thick and approximately 2.5 m apart. Between the two shear zones lies a highly fractured zone with a fracture density > 20 fracs/m. This highly fractured zone shows as a low velocity zone in seismic tomography images obtained between the AU and VE Tunnel (Fig. 2). It also correlates with a drop in P-wave velocity from 4700–4800 m/s (host rock) to 4500 m/s (Doetsch et al. 2017).

The stress measurement boreholes SBH1 and SBH3 were drilled immediately to the south of the test volume (Fig. 1), and penetrate an undisturbed rock mass characterized by an average fracture density of zero to three fractures per meter (Fig. 2a). In contrast, the borehole SBH4 shows an increasing number of brittle fractures as it approaches the S3 shear zone. Most of the structures mapped in the holes dip steeply towards S–SE, with a few dipping steeply towards WSW or ENE (Fig. 2c).

1.2 Previous Stress Data

Various stress measurement campaigns have been conducted in the Grimsel area, mostly in the context of hydropower construction projects, and in the GTS itself, in support of Nagra's nuclear waste disposal research. The campaigns included stress relief measurements (Pahl et al. 1989; Wohnlich 1999), and hydraulic fracturing tests (Pahl et al. 1989; Rummel and Klee 2009; Gruner and Ziegler 2011). Numerical models of the regional stress field have also been developed to assist the interpretation of the field observations (Konietzky and Marshall 1997) (Fig. 1). Within the GTS (BK cavern), Pahl et al. (1989)

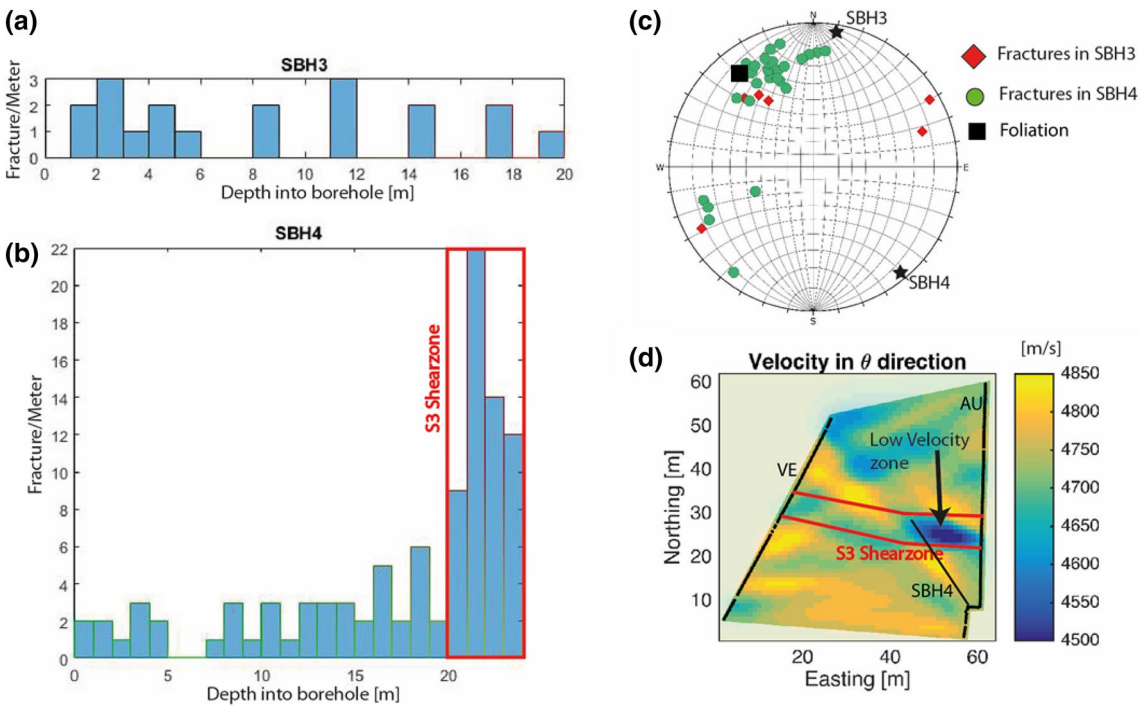

Fig. 2 Illustration of fracture densities and orientations for SBH3 and SBH4: **a** fracture densities for SBH3; **b** fracture density along SBH4, which penetrates an S3 shear zone at 20 m; **c** lower hemisphere equal angle stereonet showing orientations of fractures from SBH3 and SBH4; **d** seismic velocity tomogram between VE tunnel (left boundary) and AU tunnel (right boundary) showing the low velocity zone that lies between two S3 shear zones. Additionally, SBH4 is indicated as black line

conducted an extensive stress measurement campaign in a 191 m deep vertical borehole drilled about 300 m north of the ISC site. They performed a series of 39 overcoring tests (using 29 BGR probes and 10 CSIR triaxial cells) and 7 dilatometer tests distributed along the borehole, and 4 hydraulic fracturing tests near the hole bottom. Tests on the recovered core samples that showed the rock has a 25% elastic anisotropy. Inclusion of this in the analysis of the overcoring strains yielded stress magnitude estimates that were lower than obtained using the best-fitting isotropic elastic model. The results obtained using the anisotropic elastic model showed that $\sigma_{hmin} > \sigma_v$ above 100 m depth, and $\sigma_{hmin} < \sigma_v$ below 100 m depth. This change in stress regime reflects a drop in stress magnitude of 5–7 MPa that occurs near a hydrothermally altered open fracture zone at 100 m. The azimuth of σ_{Hmax} shows wide scatter between 45–110°, with an average in the range 90–110° (i.e., E–W to ENE–WSW strike).

Another stress measurement performed within the GTS complex was a series of slotter tests conducted in three 6 m long boreholes, two of which were vertical and one horizontal (Wohnlich 1999). These measurements aimed to measure the effect of a silo excavation on the local stress field. The reference measurement conducted at 6 m depth in one of the vertical boreholes (with a total length of approximately 6 m) prior to silo excavation revealed a σ_{Hmax} azimuth of 124° with a magnitude of 15.9 MPa.

Several other stress measurements have been conducted in the area around the GTS. Gruner and Ziegler (2011) report unpublished hydrofracture measurements by (Bühler 2011) in the 610 m deep, vertical Kessiturm borehole, drilled 2 km to the south of the GTS as part of the Grimsel III hydroelectric project. Seven hydraulic fracture stress tests were performed between 320 and 570 m depth. The σ_{min} estimates lay close to overburden stress σ_v, and the orientation of the fracture traces orientated E–W to ESE–WNW. A cluster of potential borehole breakouts identified between 568 and 581 m depth which also indicated an EW to NE–SW direction of σ_{Hmax}. Rummel and Klee (2009) conducted HF and HTPF tests between 40 and 80 m depth in a vertical borehole at Handegg, some 3.8 km north of the GTS. The results yielded an average estimate for σ_{Hmin} magnitude from ISIPs of 8.4 ± 1.2 MPa, and a roughly E–W direction of σ_{Hmax}. A general conclusion from these collective data is that σ_{Hmax} is oriented E–W to NW–SE, and that the magnitude of σ_{hmin} is close to σ_v. Thus, the stress regime is one of strike slip to thrust faulting.

Konietzky and Marshall (1997) developed numerical models of the stress field within and around the GTS site that included 3D topography to attempt to reproduce the GTS and other local stress observations. Tectonic stressing was included in their model by applying a uniform shortening between boundaries of the 3D model in the direction of the large-scale tectonic σ_{Hmax} orientation from the World Stress Map, which is roughly NE–SW. They found a σ_1 orientation (in the south of the Grimsel Test Site) of 125°/15° and a σ_3 orientation of 236°/52°, indicating that the stress tensor is likely to be rotated as a result of topography.

2 Methods

The stress measurement campaign included stress relief and hydraulic methods conducted in three boreholes with different orientations (Fig. 1), chosen largely on the average best-estimate σ_3 direction suggested by Pahl et al. (1989) and Konietzky and Marshall (1997). The SBH1 borehole was drilled downwards towards 260/75 (dip direction/downward). This borehole was dedicated to determining the orientations of the sub-horizontal principal stresses from HF traces at the borehole wall and from USBM overcoring. The SBH3 borehole was drilled sub-horizontally towards the "best-estimate" direction of σ_2 with the goal of obtaining a direct measure of the sub-vertical stress from the hydrofracture stress tests. It was drilled with a slight upward inclination (Table 1) to facilitate drainage and thus allow the use of CSIRO HI cells which must be bonded to the borehole wall with glue. The CSIRO HI tests in SBH3 provided estimates of the complete stress tensor. Both SBH1 and SBH3 were drilled into nearly undisturbed rock to the south of the experimental volume to obtain an estimate of the stresses at some distance of the large-scale faults that cut the test volume. Thus, we will refer to these estimates as the unperturbed stress. The borehole SBH4 was drilled sub-horizontally and oblique to SBH3 so as to penetrate one of the target shear zones for the stimulation conducted in the framework of the ISC experiment. The primary objective of this borehole was to quantify potential stress changes towards the shear

Table 1 Overview of SBH boreholes

Borehole	Length (m)	Diameter (mm)	Azimuth (°)	Downward gradient (°)	Mean depth below surface TVD (m)
SBH1	18.20	101	258.89	75.13	481 ± 3.4
SBH3	20.55	101	190.07	−4.91	482
SBH4	23.90	101	320.00	−5.00	482

zone with hydraulic fracturing and overcoring experiments, and to estimate the normal and shear stress acting across the fault plane.

2.1 Hydraulic Methods

In total, 11 hydraulic fracture (HF) tests (Hubbert and Willis 1957) were conducted in intervals free of natural fractures, and one HTPF measurement (Haimson and Cornet 2003) was performed on a natural fracture near a fault zone (Klee 2015). A straddle packer system was used to seal off an injection interval of 0.7 m length. Of the 11 HF tests, 9 were successful, and one failed because of suspected packer leakage (Klee 2015). Intervals free of natural fractures for HF testing were selected with the help of an optical televiewer log run shortly after drilling. A pulse test conducted before the first injection cycle was used to evaluate whether the initial interval was indeed sufficiently impermeable. The HFs were initiated during the first cycle, and subsequently propagated during multiple reopening cycles. The total injected volume for all test cycles at the different intervals ranged between 6.4 and 14 L.

The orientation of the induced fracture traces along the borehole walls was determined with an impression packer. Fracture propagation during HF tests in SBH3 and SBH4 was also traced using microseismic monitoring (see Fig. 16 for the seismic network). The seismic sensors were positioned along the tunnel walls, facing towards the test volume. During the tests in SBH3, an array of eight borehole seismic sensors was installed in SBH1. Similarly, for monitoring tests in SBH4, a sensor array was installed in a borehole parallel to the AU tunnel. The seismic sensors have a sensitivity range which is referred to as picoseismicity or acoustic emissions by other authors (e.g. Zang et al. 2017). It was shown by Guglielmi et al. (2015), that this sensitivity range is well-suitable for HF tests in crystalline rocks.

Breakdown pressure was measured during the first cycle of each HF test (Fig. 3a). The instantaneous shut-in pressure (ISIP) obtained at the end of the last reopen cycle was assumed to represent the minimum principal stress, σ_3. The ISIP was measured using the tangent method.

The HF test interval at 19.8 m in SBH4 was located at the boundary between the metabasic dyke and host rock. Owing to the complexity of the test interval, it was unclear whether a new fracture had been created or a pre-existing one had been re-opened. Thus, the interval was subjected to a step-rate test to determine the jacking pressure of the structure in the test interval (Fig. 3b).

2.2 Overcoring

A total of 16 overcoring tests were conducted, of which 10 were performed with the USBM gauge (Hooker and Bickel 1974) and 6 with the CSIRO Hollow Inclusion cell (Worotnicki and Walton 1976). CSIRO HI cells were not used in the sub-vertical borehole SBH1 as CSIRO HI cells have to be glued into a dry pilot borehole, and SBH1 could not be kept dry for the duration of glue curing. In SBH3 and SBH4, USBM and CSIRO HI tests were performed adjacent to each other. A listing of the status of all overcoring tests is presented in Table 2. Four major issues occurred during the overcoring measurements including: (1) spontaneous increase in water pressure or (2) excessive temperature increase (Fig. 17 in the "Appendix") during drilling advancement, (3) problems during extraction of overcored specimen, and (4) problems with glue curing inside CSIRO HI cell. Data considered as reliable were obtained only for four USBM overcoring and one CSIRO HI cell tests. Additionally, two CSIRO HI cells are potentially reliable

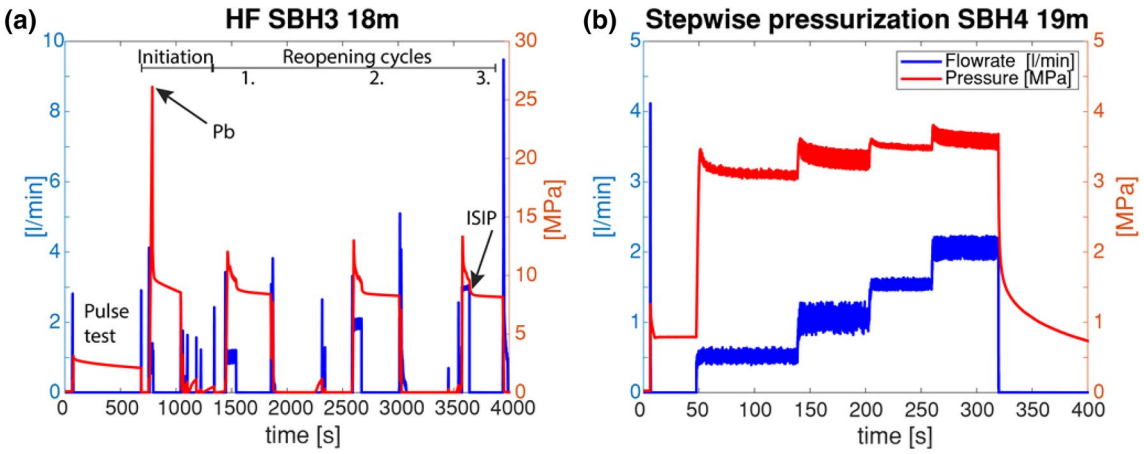

Fig. 3 Testing procedure for **a** HF tests with breakdown pressure, Pb, and instantaneous shut-in pressure, ISIP, indicated, and **b** the step-rate test conducted on the 19.8 m interval in SBH4 to estimate its jacking pressure

Table 2 Quality ranking for conducted overcoring measurements with indicated occurred problems

Testname	Depth (m)	Probe	Ranking (Bouffier 2015)	Comment
SBH1-1	10.4	USBM	1/5	Spontaneous increase by several bars in water pressure during drilling advancement
SBH1-2	11.3	USBM	1/5	Spontaneous increase by several bars in water pressure during drilling advancement
SBH1-3	12.0	USBM	1/5	Spontaneous increase by several bars in water pressure during drilling advancement and difficulties were encountered extracting the overcored specimen without damage
SBH1-4	16.0	USBM	1/5	Spontaneous increase by several bars in water pressure during drilling advancement
SBH3-1	8.3	USBM	4/5	No problem occurred
SBH3-2	9.0	CSIRO HI	4/5	Four strain gauges (B45,B135,B90 & E90) indicate abnormal behavior. They are not included in further analysis
SBH3-3	14.2	USBM	5/5	No problem occurred
SBH3-4	14.8	CSIRO HI	2/5	Increase in temperature during drilling advancement
SBH3-5	19.6	USBM	5/5	No problem occurred
SBH3-6	20	CSIRO HI	0/5	Increase in temperature during drilling advancement
SBH4-1	8.4	USBM	4/5	Orientation device moved inside overcore
SBH4-2	9.2	CSIRO HI	5/5	Increase in temperature during drilling advancement, but strain was corrected for temperature
SBH4-3	14.2	USBM	5/5	No problem occurred
SBH4-4	14.9	CSIRO HI	3/5	Increase in temperature during drilling advancement but strain was corrected for temperature. Four strain gauges indicated abnormal behavior (A0, A45, B135, C0)
SBH4-5	18.5	USBM	1/5	Difficulties were encountered extracting the overcored specimen without damage
SBH4-6	19.05	CSIRO HI	0/5	Glue cured inside the probe

although they experienced major temperature increase during drilling (Table 2). The measured strains were corrected for the temperature changes based on equations by Cai et al. 1995 and included in the analysis.

2.2.1 Estimation of Elastic Parameters

The inversion of overcoring strain recordings to estimate stress requires an estimate of the elastic properties of the core. Immediately after each overcoring test, the core was extracted from the borehole and tested on-site in a biaxial test apparatus (Bouffier 2015). The hollow-rock cylinders with the probes inside were subjected to two loading/unloading cycles up to 12 MPa, and the corresponding loading/unloading strains measured by the gauges of the probe. As a first step in estimating the elastic parameters of the core from the biaxial data, we followed other authors in assuming an isotropic elastic rock model (Bjarnason et al. 1988; Christiansson and Janson 2003). However, the rock in question is known to have a significant elastic anisotropy and is well-described by a transversely isotropic rock model. Thus, we developed a new method for estimating the five independent elastic parameters required to parametrize such a model, which could then be used to invert the CSIRO HI cell strains recorded during overcoring. The method was based on a three-dimensional simulation of the biaxial tests using the finite element package COMSOL Multiphysics. The five parameters include the Young's moduli parallel and perpendicular to the plane of isotropy, denoted as E_1 and E_2, respectively, the corresponding Poisson ratios ν_{21} and ν_{31}, and the so-called independent cross-shear modulus G_{12}. It is not possible to infer all of them from one biaxial test, because the problem is underdetermined.

The 3D finite element model of the biaxial test assumes the overcored sample is composed of transversely isotropic, linear elastic material, and is shown in Fig. 4. The simulated CSIRO HI cell strain gauges were located approximately 30 cm away from the free face of the core, similar to the real field situation. At the position of the strain gauges, the size of the mesh grid was 0.48 mm × 0.27 mm per element. The hollow cylinder was loaded along its entire outer lateral surface by 12 MPa (Fig. 4). The orientation of the foliation inside the overcore was taken to represent the plane of isotropy of the coordinate system used to define the transversely isotropic medium. The model was applied to simulate the biaxial test to estimate the transversely isotropic elastic parameters of the rock. In reality, the elastic parameters obtained will reflect the combined properties of the rock, the CSIRO HI cell material, and the glue. However, the approximation introduced by not explicitly including the bonded cell in the simulator is acceptable, as it is the combined properties that are needed to invert the overcoring strains for the stresses. (Note that the transversely isotropic parameters thus obtained are not precisely representative of the rock.) Nevertheless, the strain gauges in the model were located at the exact position they would be had the CSIRO HI cell been

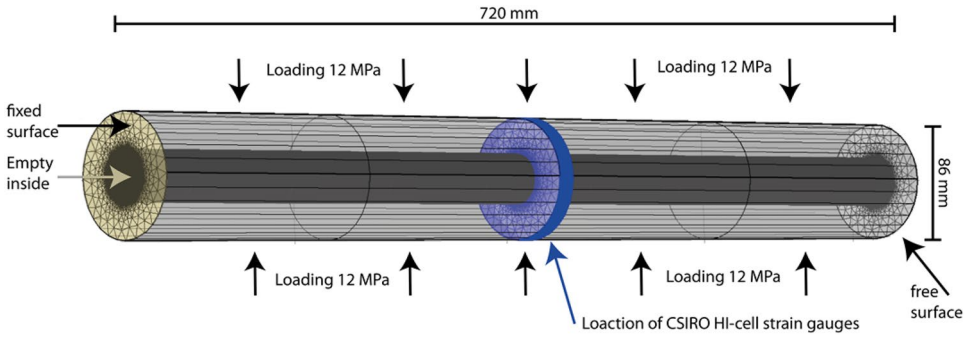

Fig. 4 Three-dimensional finite element model of the biaxial test. Loading of lateral surfaces is indicated (black arrows), as well as the position of the CSIRO HI cell strain gauges (blue area) and fixed surfaces (light yellow). (Color figure online)

explicitly included in the model. One face of the cylinder in the simulator was fixed (unlike the real biaxial test) to ensure model convergence. However, the cylinder length was chosen sufficiently large to avoid boundary effects.

The five independent elastic parameters were varied with a grid search approach to find the combination that gave a best fit between the modelled and measured CSIRO HI cell strains. The root-mean-squared (RMS) sum of the differences between the modelled and measured strain gauges was used as a measure of fit quality. The following assumptions were made to limit the number of simulations:

(a) The two Young's moduli were related as:

$$E_2 = \lambda \times E_1 \tag{1}$$

with λ representing the factor of anisotropy. Uniaxial tests conducted on core plugs taken from near the overcoring tests indicated that $\lambda = 0.5$ (Fig. 18 in "Appendix"). Thus, $\lambda = 0.5$ was taken as the preferred value, although it was allowed to range between 0.4 and 1 in sensitivity studies that were conducted to evaluate its effect on the stress tensor solutions.

(b) The independent shear modulus, G′, was approximated using the empirical equation (Saint–Venant 1863; Worotnicki 1993)

$$G' = \frac{E_1 \times E_2}{E_1 \times \left(1 + 2 \times \nu_{12}\right) + E_2} \tag{2}$$

(c) The Poisson's ratio for the rock lies between 0.25 and 0.37 (Keusen et al. 1989; Pahl et al. 1989).

The overall parametric grid (including elastic parameters and anisotropy factors) contained in total 2025 models.

2.2.2 Inversion for Stresses

The strains recorded during the overcoring tests were inverted for the stresses using the compliance matrix obtained from biaxial tests. The inversion utilized the CSIRA code by (Amadei 2000), which is based on the equations provided by Amadei and Stephansson (1997). The code calculates least-square estimates of the principal stress components (i.e., magnitude and orientation) of the 3D in situ stress field. Since the inversion is overdetermined due to the 12 strain gauges of the CSIRO HI cell, there is some, albeit limited scope to neglect the data from strain gauges that show clear evidence of abnormal behavior, such as might result from poor bonding (see comments in Table 2).

In the first step of the analysis of the overcoring strains, an isotropic elastic rock model utilizing the elastic parameters estimated from the biaxial test was used for the inversion (i.e., Young's modulus and Poisson's ratio).

In the second step, the overcoring strains were analyzed with the transversely isotropic model whose parameters were subject to wide variation to evaluate their effect on the resulting stress tensor. The model of Amadei (2000) was used for the inversion. The factor of anisotropy, λ, varied between 1 and 0.4 (i.e., isotropic to highly anisotropic), E_1 was kept constant at 21 GPa, and the Poisson's ratios varied between 0.15 and 0.33. This step will be referred to as the 'preliminary sensitivity study'.

In the third step, a 'constrained' sensitivity study was performed, again with the transversely isotropic model, but this time using only those parameter sets which, when used to parametrize the simulator of the biaxial test, yielded a lower RMS than was obtained with the best-fitting isotropic parameter set. Thus, the first stage in this step was to identify the parameter combinations that yielded a sufficiently low RMS by conducting a grid search with the biaxial test simulator.

Table 3 Input parameters for sensitivity study

Parameter	Value
λ	0.5, 0.625, 0.75, 1, (additional for SBH4-4: 0.4, 0.45)
E_1 (GPa)	17, 19, 21, 23, 25
υ_{12}	0.15, 0.19, 0.21, 0.25, 0.29, 0.30, 0.33
υ_{13}	0.15, 0.19, 0.21, 0.25, 0.29, 0.30, 0.33

E_1 was varied between 17 and 25 GPa for this analysis. The ranges of all parameters used is given in Table 3.

3 Results

3.1 Hydraulic Methods

The HF test results are listed in Table 4. The breakdown pressures obtained from tests in the relatively undisturbed rock of SBH1 and SBH3 ranged from 19 to 25 MPa with systematically lower values in SBH1. The values observed along SBH4 progressively decreased from 22.5 MPa at 9 m to values below 15 MPa as a major S3 shear zone was approached at 19.7 m (Fig. 5a; Table 4). In SBH1 and SBH3, the ISIPs varied between 8 and 9.6 MPa (Fig. 5b). These values were assumed to represent reliable measures of σ_3 magnitude in the relatively undisturbed rock south of the test volume. In SBH4, the ISIP decreased from 8.0 to 2.1 MPa as the S3 shear zone was approached. Since the latter was so low, a step-rate fracture-opening test was conducted which indicated a jacking pressure of 2.8 MPa (Fig. 5c). The latter is taken as the best measure of σ_3.

Table 4 Overview results of HF and HTPF

Test name	Breakdown pressure (MPa)	ISIP (MPa)
SBH1 8.0 m depth	18.0	8.3
SBH1 11.0 m depth	19.8	9.2
SBH1 13.0 m depth	13.8	9.6
SBH1 15.0 m depth	19.2	9.2
SBH3 8.0 m depth	23.4	8.1
SBH3 13.0 m depth	25.7	8.8
SBH3 18.0 m depth	26.1	9.1
SBH4 9.0 m depth	22.7	8.0
SBH4 15.95 m depth	13.5	6.5
SBH4 17.8 m depth	13.5	5.3
SBH4 19.8 m depth	10.3	2.8 (jacking pressure)

An impression packer test was conducted after each HF test in SBH1 and SBH3. The fracture traces in the sub-vertical SBH1 borehole were almost axial and dipped steeply towards south (average dip direction/dip 173/81). The fractures' orientations implied by the traces cut the foliation plane at an angle of about 40°. Thus, we provisionally assume that they propagated under stress control in a plane normal to σ_3. In SBH3, the two successful impression packer tests indicated non-axial fracture traces that formed in the foliation plane, which OPTV logs showed dipped steeply towards SE (average dip direction/dip 140/71). Although these two fractures clearly initiated in the foliation plane, the microseismic evidence summarized below indicates that they rapidly rotated to propagate in a plane that was parallel to the mean orientation of fractures in SBH1.

The HF tests in SBH3 and 4 induced numerous microseismic events that were recorded on the sensor arrays. The seismic monitoring of HF tests in SBH1 was not successful owing to pump noise and network geometry. The hypocenters of the events induced during the SBH3 and 4 tests obtained by JHD using a transversely isotropic p-wave velocity model with 7% anisotropy are shown in Fig. 6 (Gischig et al. 2018). Only events that were recorded on three sensors along the tunnel walls and on the borehole array were included in the localization procedure to reduce network bias (Gischig et al. 2018). The hypocenters of the three SBH3 tests defined three oblate, steeply dipping clouds that initiated in the injection intervals and consistently propagated in an EW direction. High-precision relocation of subsets of events in each cloud that had similar

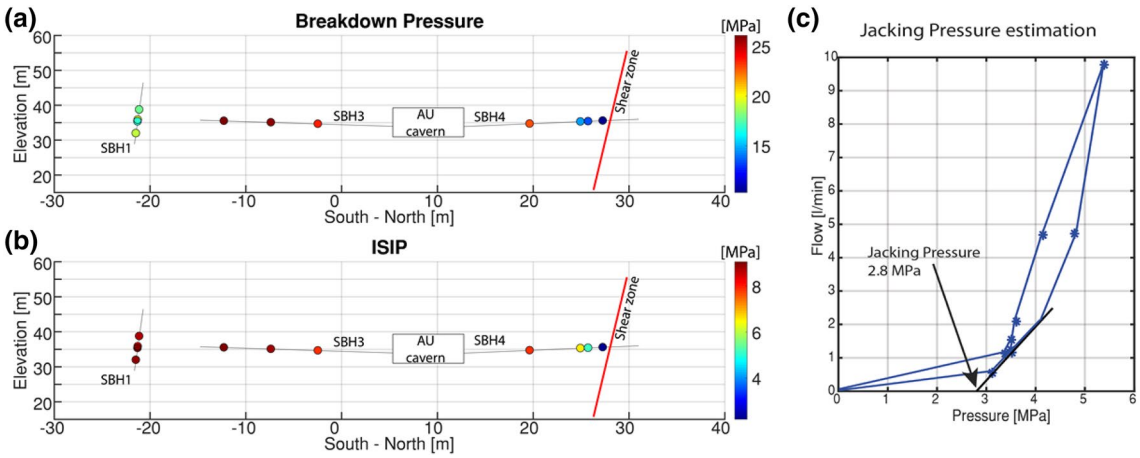

Fig. 5 Location of the HF experiments, viewed towards west into the test volume, with a color-coded indication of **a** breakdown pressure and **b** ISIP. Frame **c** shows the estimation of the jacking pressure (**c**) from the step-rate test conducted at 19.7 m in SBH4 after the HF test. (Color figure online)

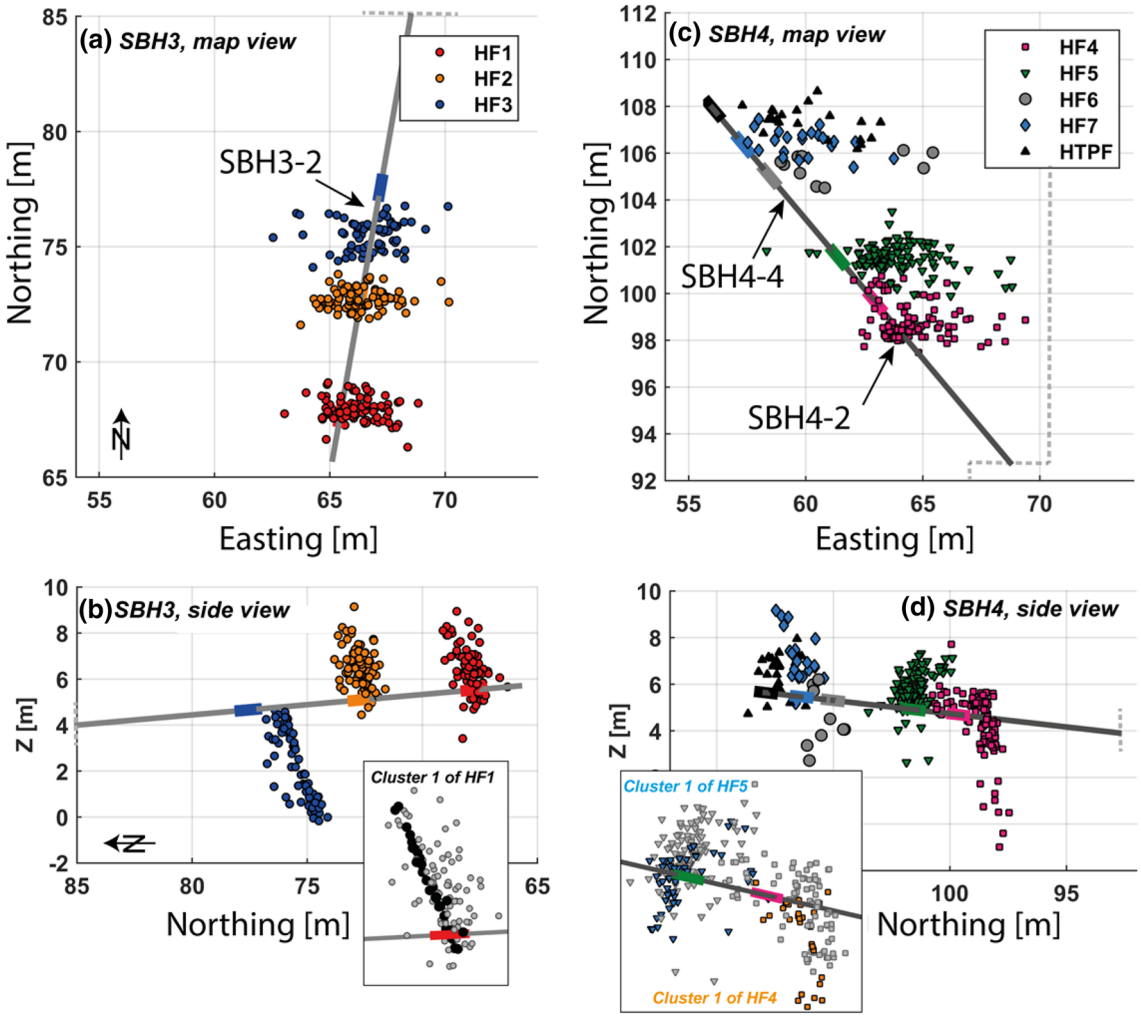

Fig. 6 **a–d** Hypocenters of events recorded during the HF experiments located with JHD. Each color represents one HF experiment. The insets show high-precision relative locations of events within clusters that have a similar waveform. **a, b** Modified after Gischig et al. (2018)—**c, d** are produced following the same procedure as presented by Gischig et al. (2018). Additionally, cluster 1 is shown for HF1, HF4 and HF5. This naming corresponds to the naming in **a–d**

waveforms revealed narrow seismic structures parallel to the planes of the clouds that were taken to represent the propagation planes of the SBH3 fractures away from the well (Gischig et al. 2018). The average dip and dip direction of planes fitted through these structures was ~ 185/75 (see inset of Fig. 6). The pole to this average orientation of 005/15 is shown in Fig. 7, and can be seen to coincide with the mean orientation of the poles of the four SBH1 hydrofracture traces which scatter ± 20° about it. This supports the view that although two, and possibly three of the SBH3 hydrofractures initiated in the foliation plane under the control of the tensile strength anisotropy, they rapidly rotated during propagation under stress control to adopt an orientation that was normal to σ_3. Thus, we take σ_3 to point towards 005/15 (Gischig et al. 2018). Since the seismic clouds extend up to the wellbore, and show no evidence of a change in orientation as the wellbore is approached, the rotation must have occurred within a few decameters of the wellbore (Gischig et al. 2018).

The seismicity clouds in SBH4 also propagated roughly EW, but showed a less clear oblate geometry than the seismic clouds in SBH3. Precise relocation of clusters of events with similar waveform found within the clouds induced by two of the SBH4 injections revealed seismic structures that had a more diffusive appearance and did not illuminate distinct fractures as clearly as in SBH3 (see seismic cloud orientations in Table 5). It was not clear if this was: (1) an artifact of the monitoring network having a geometry that was more optimal for locating events near SBH4 than for SBH3; (2) related to an increase in pre-existing fracture density in SBH4 (Fig. 2) leading to more complex fracture propagation, or (3) related to the change in the stress field

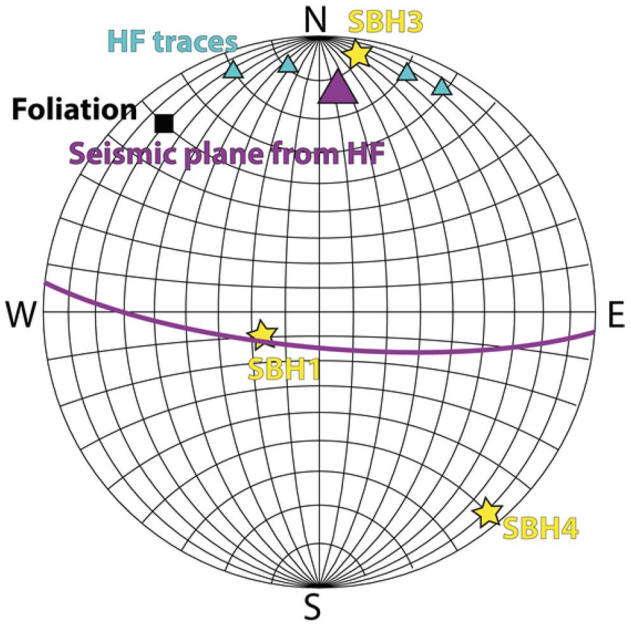

Fig. 7 Lower hemisphere equal angle stereonet showing pole points of HF traces, the seismic plane and the foliation

Table 5 Recorded seismic clouds during HF tests

HF test	Borehole	Orientation (dip direction/dip)
HF1	SBH-3	180/72
HF2	SBH-3	175/76
HF3	SBH-3	178/69
HF4	SBH-4	185/73
HF5	SBH-4	001/65
HF6	SBH-4	162/64
HF7	SBH-4	185/73
HTPF	SBH-4	010/79

The data for HF1-3 were taken from Gischig et al. (2018), and data for tests in SBH-4 from Näf (2017)

along SBH4 shown in Fig. 5. Nevertheless, the seismicity clouds and the clusters they contain were oblate structures that extended in an EW direction and could be divided into two sets depending upon dip: (a) steeply dipping towards south and therefore parallel to the clouds in SBH3, and (b) steeply dipping towards north. The EW extension is consistent with the seismic structures in SBH3, and is taken to indicate the fractures propagated into EW direction.

The traces of induced fractures along the SBH1 borehole are consistent with the orientation of the plane fitted through the seismic cloud from SBH3 with a deviation of ±30° in strike (Fig. 6e). As mentioned above, the fracture traces in borehole SBH3 were almost parallel to the average foliation plane (i.e., deviation < 20°). Gischig et al. (2018) propose that the fracture initiated along foliation, and then quickly rotated to propagate in a high-angle plane with EW strike that was normal to σ_3.

3.2 Overcoring

3.2.1 USBM probe

The results obtained from the on-site biaxial tests of the USBM overcore at 8.3 m in SBH3 and the CSIRO HI cell overcore at 9 m in SBH3 are shown in Fig. 8a. These data are representative of the typical response obtained during the biaxial re-loading of overcore cylinders during the field campaign. The strains for the USBM test clearly indicate anisotropic elastic rock properties because gauge 3 shows markedly larger displacements than gauges 1 and 2 which are similar. Nevertheless, the analysis of the USBM data, both from the biaxial test and the overcore itself, assumed an isotropic rock model. The isotropic elastic modulus was estimated by taking simple averages of the three displacement curves obtained from each biaxial test (Bouffier 2015). The resulting Young's Modulus estimates from all tests ranged between 22.0 and 30.5 GPa.

The data from the USBM probes constrain the magnitudes and orientations of the maximum (σ_{Max}) and minimum (σ_{min}) stress components in the plane normal to the borehole. In SBH3, the σ_{Max} magnitudes were relatively consistent, varying between 12 and 13.2 MPa, whereas the σ_{min} estimates increased slightly from 7.8 to 10.6 MPa with increasing depth into the borehole. The range in the magnitudes also coincides with a variation in Young's moduli obtained from the biaxial tests. The USBM test in SBH4 at 14.2 m that was ranked as '5/5' (Table 2) yielded σ_{Max} and σ_{min} estimates of 7.8 MPa and 6.6 MPa, respectively. Both these magnitude values are smaller than the ones measured in SBH3, which is not consistent with a uniform stress field, even though the boreholes are oriented differently. The orientations of the stresses in the plane normal to SBH3 indicated an east dipping σ_{Max}, the dip angle increasing from 1° to 43° at greater depth in the borehole (Fig. 9). The dip of σ_{Max} indicated by the USBM test in SBH4 at 14.2 m was also 30° towards east. The σ_{Max} orientations from USBM tests have an estimated accuracy of ±30°, due to their gauge distribution around the probes circumference.

3.2.2 CSIRO HI cell

3.2.2.1 Results of Isotropic Inversion Only three CSIRO HI cell tests yielded results that were considered reasonably reliable (ranked as 3/5–5/5) (see Table 2), and so only these tests were analyzed. Although the stress–strain curves showed clear evidence of elastic anisotropy (e.g., Fig. 8b), an isotropic rock model parametrized with the iso-

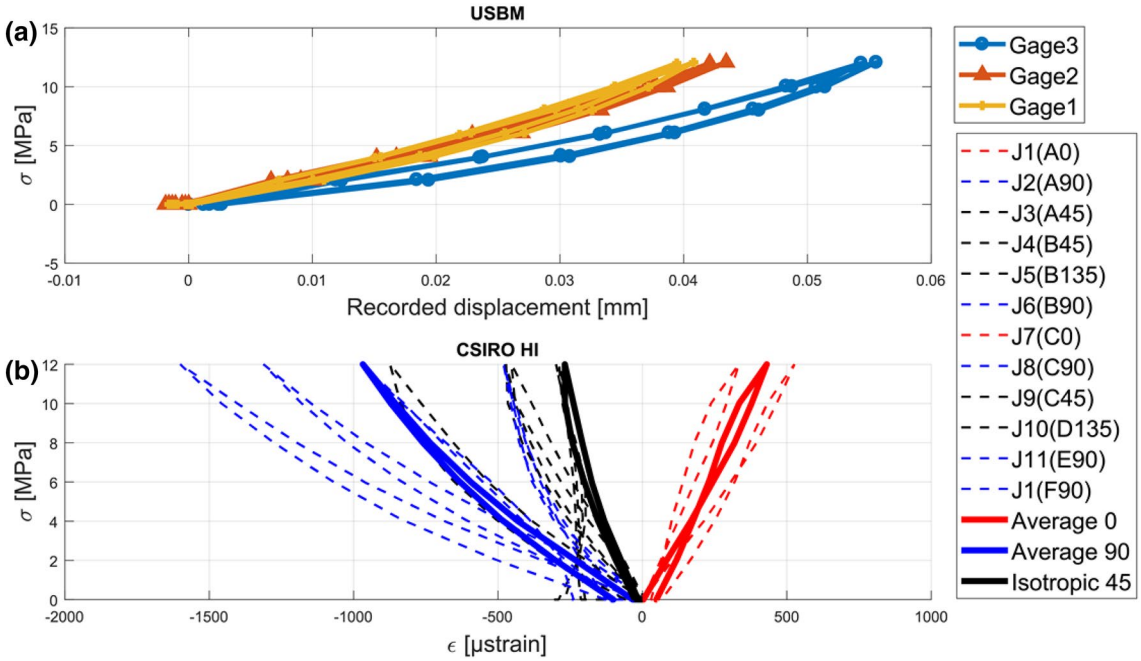

Fig. 8 Results from the in situ biaxial tests. **a** USBM stress-displacement (i.e., change in diameter of EX-hole) curves from the test on the overcore at 8.3 m in SBH3. **b** Strain curves from the CSIRO HI cell during the overcore in SH4 at 9.0 m. The symbols distinguish between the different strain gauge orientations, and the bold lines indicate the average orientations for axial and circumferential strain gauges and the expected isotropic loading path of the oblique gauges

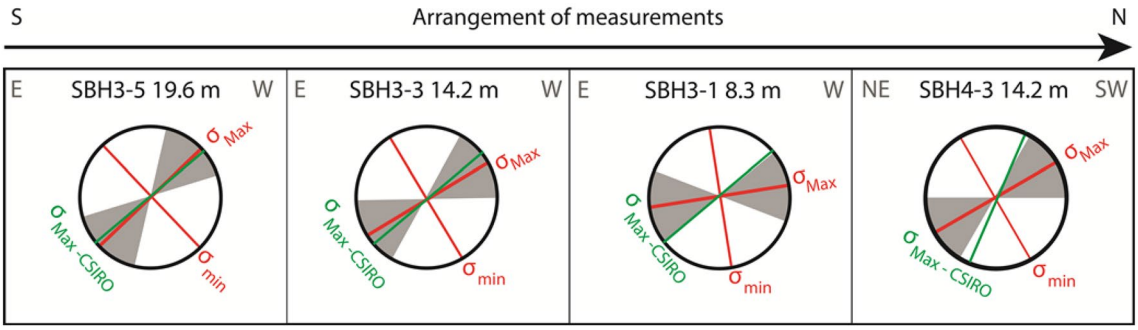

Fig. 9 Orientations of σ_{Max} and σ_{min} plotted looking into the boreholes for SBH3 and out of the borehole in SBH4 (view towards South). The accuracy of the measured orientation is indicated by the gray area with covers orientations ± 30° around the obtained orientation. The σ_{Max} calculated from the corresponding CSIRO HI cells are shown in green. (Color figure online)

tropic elastic moduli was used as a first step in the analysis. The isotropic elastic parameters from biaxial testing of the CSIRO HI cell overcores were estimated in a different way to the simple averaging used for the USBM test. Specifically, a grid search was conducted using the aforementioned numerical simulator (Fig. 4) to find the Young's modulus/Poisson's ratio pair that yielded the lowest RMS discrepancy between predicted and observed strains. For an isotropic material, the independent parameters for the simulator are $E_1 = E_2 = E$, $\lambda = 1.0$, $\nu_{12} = \nu_{12} = \nu$, and G′ is the standard shear modulus. The parameter estimates computed in this way for each of the three tests are listed in Table 6 together with the associated RMS values. The Young's modulus estimates ranged between 19 and 21 GPa, which compares with

Table 6 Overview elastic parameters for an isotropic rock model based on biaxial simulator

Measurement	$E_1 = E_2 = E$ (GPa)	$\nu_{12} = \nu_{12} = \nu$	G = G′ (GPa)	RMS
SBH3-2	21	0.33	7.895	165.55
SBH4-2	21	0.33	7.895	159.87
SBH4-4	19	0.33	7.143	343

a range of 20.4–25.7 GPa obtained by simple averaging of the displacement curves (Bouffier 2015), and the Poisson's ratio estimates were consistently 0.33, which compares with 0.24–0.27 obtained from the simple averaging method. The isotropic parameter estimates obtained with the grid search method are preferred because they represent true best fits to the biaxial test data.

The principal stress estimates obtained by inverting the overcoring strains with the model of (Amadei 2000) using the best-fitting isotropic parameter estimates are shown for all CSIRO HI tests in Fig. 10a (left column of Fig. 10). In all three cases, the principal stress orientations are reasonably consistent. The major principal stress (σ_1) pointed sub-horizontally towards SE (i.e., the azimuth ranges between 141–144°) (Fig. 10a), which was sub-parallel to the SBH4 borehole (i.e., 140/05, dip direction/dip). The intermediate (σ_2) and minor principal stresses (σ_3) were steeply inclined and dipped towards NE and SW, respectively. The σ_1 magnitude estimates range between 20.3 and 23.3 MPa depending upon the test, and were significantly greater than the corresponding estimates for both σ_2 and σ_3 which ranged between 8.7 and 15.3 MPa, the maximum difference between σ_2 and σ_3 being 3.1 MPa.

3.2.2.2 Unconstrained and Constrained Transversely Isotropic Sensitivity Analyses *Preliminary sensitivity study* The preliminary sensitivity study examined the dependence of the stress estimates derived from the three reasonably reliable CSIRO Hi cell tests on the two values of Poisson's ratio, ν_{21} and ν_{31}, and the factor of anisotropy, λ. Young's modulus, E_1, was held at 21 GPa. The results showed that the elastic parameter values used had a large impact on the stress estimates. The principal stress orientations obtained from the different parameter combinations are shown in Fig. 10b. For the SBH3 test, the orientations migrate over a large range which is largely controlled by the factor of anisotropy, the values of the Poisson's ratios having a minor effect. The orientation of σ_1 rotates from SE to E as the anisotropy factor was increased (see arrow on σ_1 path in Fig. 10b). The magnitude of σ_1 ranged from 11 to 19 MPa, σ_2 ranged from 8 to 16 MPa,

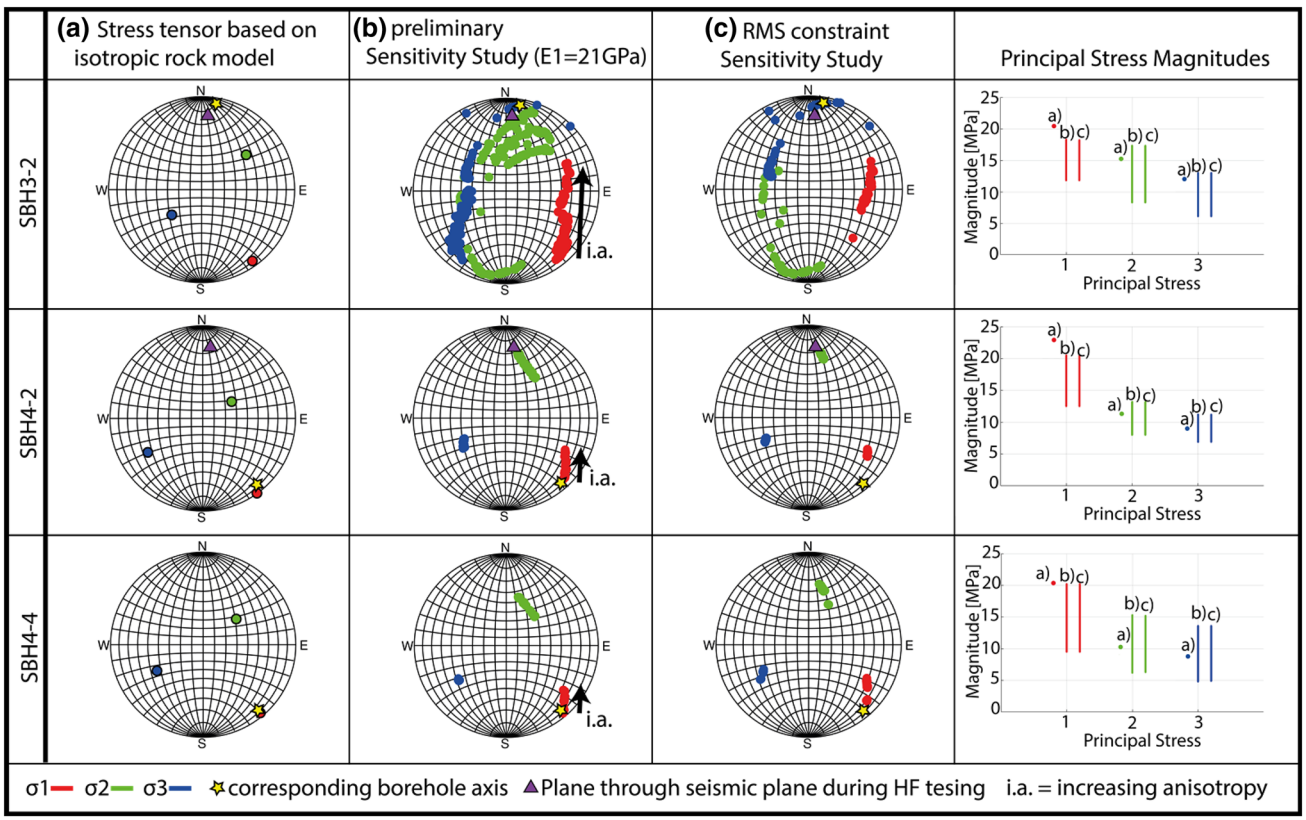

Fig. 10 Principal stress tensors obtained from CSIRO HI overcoring in SBH3 and SBH4. The left three columns show the principal axis orientations on a lower hemisphere, equal angle projection obtained for **a** the isotropic rock model; **b**, the preliminary sensitivity analysis using a transversely isotropic rock model and a broad range of parameter variation; and **c**, the 'constrained' analysis using the limited range of parameter values that yield lower RMS discrepancies when applied to the biaxial test than obtained with the isotropic model. In all plots, the borehole orientations and average orientation of the poles to the planes of the seismic structures induced during the HF injections are also plotted. The arrow drawn on the trace of the σ_1 solutions in column (**b**) denotes the effect of increasing the factor of anisotropy. The column at right shows the magnitudes of the principal stresses for the three sets of analyses

and σ_3 from 6 to 13 MPa. In contrast, for the two SBH4 tests, the orientation of the principal axes showed less variation, the σ_1 orientation deviating only slightly from alignment with the SBH4 borehole axis for both tests (Fig. 10b). The magnitude of σ_1 ranged between 21 and 9 MPa, σ_2 ranged between 15 and 7 MPa, and σ_3 between 13 and 4 MPa.

Constraints on transversely isotropic parametric values from the biaxial tests The ranges of the anisotropic elastic parameters were constrained for each of the three reasonably reliable CSIRO HI Cell measurements by modelling the biaxial tests with the numerical simulator and monitoring the RMS discrepancies between modelled and measured strains. The ranges of variation of the five parameters are listed in Table 3. The RMS values obtained for the various combinations of the parameters are shown for each test in Figs. 19, 20, 21. All three tests indicated similar behavior in terms of sensitivity with respect to parametric variations. All models indicated a decrease in RMS towards an anisotropy factor of 0.5 and an E_1 Young's modulus of around 21 GPa. However, the Poisson's ratios, ν_{12} and ν_{13}, were not well–constrained, as the RMS minima were broad and not well-defined. Thus, in the subsequent inversions of the overcoring strains, both Poisson's ratios were allowed to range from 0.25 to 0.37. Depending upon the CSIRO HI test, some 100–200 solutions were found that yielded RMS values better than the corresponding threshold RMS obtained with the best-fitting isotropic elastic parameter sets (Table 6). Solutions at the boundary of the grid that had Poisson's ratios outside the range of values considered acceptable of 0.25–0.37 were excluded. The resulting constrained ranges of the transverse isotropic parameters are given for each CSIRO HI test in Table 7. It is evident that both E_1 and E_2 are constrained to values that are smaller than those derived from the on-site biaxial tests, although the range of the anisotropy factor was consistent with the value obtained from the uniaxial compressive tests on core plugs.

Constrained Sensitivity Study

Using the constrained, transversely isotropic, elastic parameter ranges listed in Table 7, the inversion of the overcoring strains from test SBH3-2 yielded estimates for principal stresses shown in Fig. 10c. The magnitude of σ_1 ranged from 11 to 19 MPa, σ_2 ranged from 8 to 16 MPa, and σ_3 from 6 to 13 MPa. The orientation of σ_1 dipped at ~40° in a direction that ranged between ENE and ESE. The orientations of σ_2 and σ_3 point towards S to W, and WNW to N, respectively (Fig. 10c). Comparison of Fig. 10b, c shows that the constrained parameter set results in a significant improvement in the constraints on the principal stress orientations. However, this additional measure did not improve the constraint on the stress magnitudes. Note that the stress solutions in Fig. 10c differ from the solution presented by Krietsch et al. (2017). This is due to the use of the true best-fit isotropic elastic parameters (RMS constraint) in this paper, whereas Krietsch et al. (2017) used the on-site estimated isotropic elastic parameters given by Bouffier (2015).

For the two CSIRO HI cell tests performed in SBH4, inversion with the respectively constrained parameter sets (Table 7) gave σ_1 orientation estimates that in both cases were well-constrained (Fig. 10c). Additionally, the positions of σ_2 and σ_3 were exchanged with respect to SBH3 (Fig. 10c). The magnitude of σ_1 ranged between 21 and 9 MPa, σ_2 ranged between 15 and 7 MPa, and σ_3 between 13 and 4 MPa.

It should be noted that the σ_1 orientation obtained for the SBH4-4 test was found to be sub-parallel to the borehole axis, which in principle could be diagnostic of glue problems, perhaps promoted by thermal effects. The temperatures of both the SBH4-4 and SBH4-2 cells increased by 10 °C during overcoring, and these were corrected for in the analysis (Bouffier 2015). However, the correction does not include potential glue creep. Four gauges of SBH4-4 showed abnormal behavior and were discounted from the analysis, although no anomalous gauges were identified for SBH4-2. For this reason, the results from SBH4-4 are considered less reliable than SBH4-2, which did not indicate alignment of the σ_1 orientation with the borehole axis (i.e., 25° difference).

Table 7 Output parameter from grid search based on RMS constraint

	SBH3-2	SBH4-2	SBH4-4
λ	0.5, 0.625	0.5, 0.625	0.40., 0.45
E_1 (GPa)	19, 21, 23	21, 23	21, 23, 25
V12	0.15, 0.19, 0.21, 0.25, 0.29, 0.30, 0.33	0.15, 0.19, 0.21, 0.025, 0.29, 0.30, 0.33	0.19, 0.21, 0.29, 0.30, 0.33
V13	0.15, 0.19, 0.21, 0.25, 0.29, 0.30, 0.33	0.15, 0.19, 0.21, 0.025, 0.29, 0.30, 0.33	0.15, 0.19, 0.21, 0.025, 0.29, 0.30, 0.33

4 Integration of Methods

The complete determination of all primary stress components at one or more locations of a given site is a challenging task requiring iterative data integration (e.g., Stephansson and Zang 2015). Notwithstanding the availability of generic strategies for such, the details of the approach to be taken must be adjusted to site specificities and to the type and characteristics of available data. In the following, we propose an integration approach that appears to be appropriate for our site. Our approach was driven by the following site and data specificities:

Our site is traversed by brittle shear zones that could be associated with local disturbance of the stress field. Thus, we integrate our data in two steps: first, we consider only data away from the shear zones to derive a so-called "unperturbed stress field"; second, we examine data obtained within and near the shear zones to obtain a "perturbed stress field".

Note that all measurements are made sufficiently far away from tunnels and other cavities to be unaffected by the stress redistribution occurring around them.

Our rock type is anisotropic due to an alpine foliation, which reflects a preferential alignment of phyllosilicate minerals. Such mechanical and elastic anisotropy can potentially affect both the results of the overcoring and the hydraulic fracturing data, and will increase the number of model parameters, which in turn will increase the uncertainty in the stress determination. Note that the anisotropy we consider is a primary anisotropy, i.e., it is related to the natural rock fabric, and does not develop as a secondary response due to stress relief microcracking related to drilling and sampling, as sometime observed in deep boreholes (e.g., Zang et al. 1996; Yaméogo et al. 2013). Indeed, our site is relatively shallow and the rock is relatively strong. For these reasons we assume that its strength to stress ratio is sufficiently high and microcracking effects during our stress measurements can be neglected.

Not all stress components can be evaluated with the same level of confidence. For example, the minimum stress magnitude can be derived relatively directly from hydraulic fracture tests and thus will be determined more confidently than the maximum principal stress magnitude. This consideration underlay our stress estimation approach in which we sought to constrain the inversion process to reduce the number of consistent and acceptable solutions.

4.1 Unperturbed Stress Field Based on Transverse Isotropic Rock Model

The stress tensor derived by inverting the SBH3-2 CSIRO HI-cell overcoring strains with the isotropic model (Fig. 10a) indicates an σ_3 orientation that dips steeply towards SW. Since this is not consistent with the pattern of seismicity induced during HF, which suggests that σ_3 is sub-horizontal and oriented N–S, we investigated whether the discrepancy could be alleviated using a transversely isotropic model in the inversion of the overcoring strains. The constrained sets of the transversely isotropic elastic parameters given in Table 7 yielded the stress solutions for the SBH3-2 data shown in Fig. 10c. Some are evidently now consistent with the σ_3 direction obtained from HF and microseismic monitoring (Fig. 10c), although the range spanned by the solutions is large. To reduce the range further, an additional constraint arising from the hydrofracture tests (HF) was implemented. Specifically, it was noted that the σ_3 magnitude estimates derived from the HF tests, which are considered to represent ground truth, never exceeded 9.6 MPa in boreholes SBH1 and SBH3, both of which penetrate rock where the stress is considered to be unperturbed. Thus, the SBH3-2 overcoring solutions in Fig. 10c were additionally constrained by retaining only those that satisfied $\sigma_3 \leq 9.6$ MPa. The resulting constrained range of solutions is shown in Fig. 11a.

Evidently, the range of orientations and magnitudes of admissible solutions is now significantly reduced. The orientation of σ_1 is better constrained, whilst those of σ_2 and σ_3 range around a great circle in a manner that is consistent with the indicated similarity of their magnitudes. Importantly, the range of σ_3 extends to include the pole to the plane of the microseismic clouds induced during the SBH3 injections. As noted earlier, since these clouds are all reasonably planar, and essentially parallel to each other in an orientation that is unrelated to structure or fabric within the rock mass, it is likely that they formed under stress control in a plane normal to σ_3. Moreover, the consistency in the orientation of the planes suggests that the magnitude of σ_3 is decidedly less than σ_2, but that the difference is not resolved by the analysis of the SBH3-2 test. Accepting this, a further constraint was implemented by retaining only those solutions in Fig. 11a whose σ_3 orientation lay within 20° of parallel to the pole of the best-fitting plane to the SBH3-2 microseismic cloud (i.e., HF3 in Fig. 6) yielding the distribution shown in Fig. 11b. The best estimate of the stress tensor for SBH3 was obtained by tensor averaging of these solutions, and the result is plotted in Fig. 12 and listed in Table 8. Note that the estimate of σ_3 of 8.7 MPa is reasonably consistent with the average σ_3 from the seven hydrofracture tests in SBH1 and SBH3 of 8.9 MPa. We will refer to this as the unperturbed stress tensor, as the measurements were made in unperturbed rock.

It is evident that σ_3 of the best-fit CSIRO HI-derived tensor for SBH3 is approximately parallel to the borehole axis. Thus, the stress components, σ_{Max} and σ_{min} obtained from the USBM probes in SBH3 should provide a reasonably direct measure of σ_1 and σ_2 in terms of orientation and magnitude. Support for this is given by the reasonable consistency of the orientations of σ_{Max} and σ_{min} with σ_1 and $\sigma_{2,}$ respectively, as shown in Fig. 11b. The σ_{Max} and σ_{min} magnitude estimates of 12.0–13.2 MPa and 7.8–10.6 MPa, respectively, also compare favorably with the estimates of σ_1 and σ_2 from the constrained SBH3-2 CSIRO HI solutions (Fig. 11), although the σ_1 values may be slight overestimated if the boreholes were not perfectly parallel to σ_3. The final USBM-derived stress components yielded σ_{Max} and σ_{min} magnitudes of 12.63 and 9.29 MPa, respectively, based on tensor averaging. The averaged orientations are plotted in Fig. 11.

The vertical stress, σ_{zz}, resolved from the unperturbed stress tensor was found to be 10.7 MPa. This is in reasonable agreement with the estimated overburden of 12.24 MPa for a depth of 480 m and a rock density of 2600 kg/m^3, given that the topography above the site is severe.

The unperturbed stress tensor from the overcoring tests in SBH3 is shown in Fig. 12 together with the poles to the fracture traces induced during the hydrofracture measurements in SBH1. The traces of the HF measurements in SBH3 are not considered here as their orientation was predominantly influenced by the foliation plane rather than the prevailing stress state (Gischig et al. 2018). The poles to the HF traces

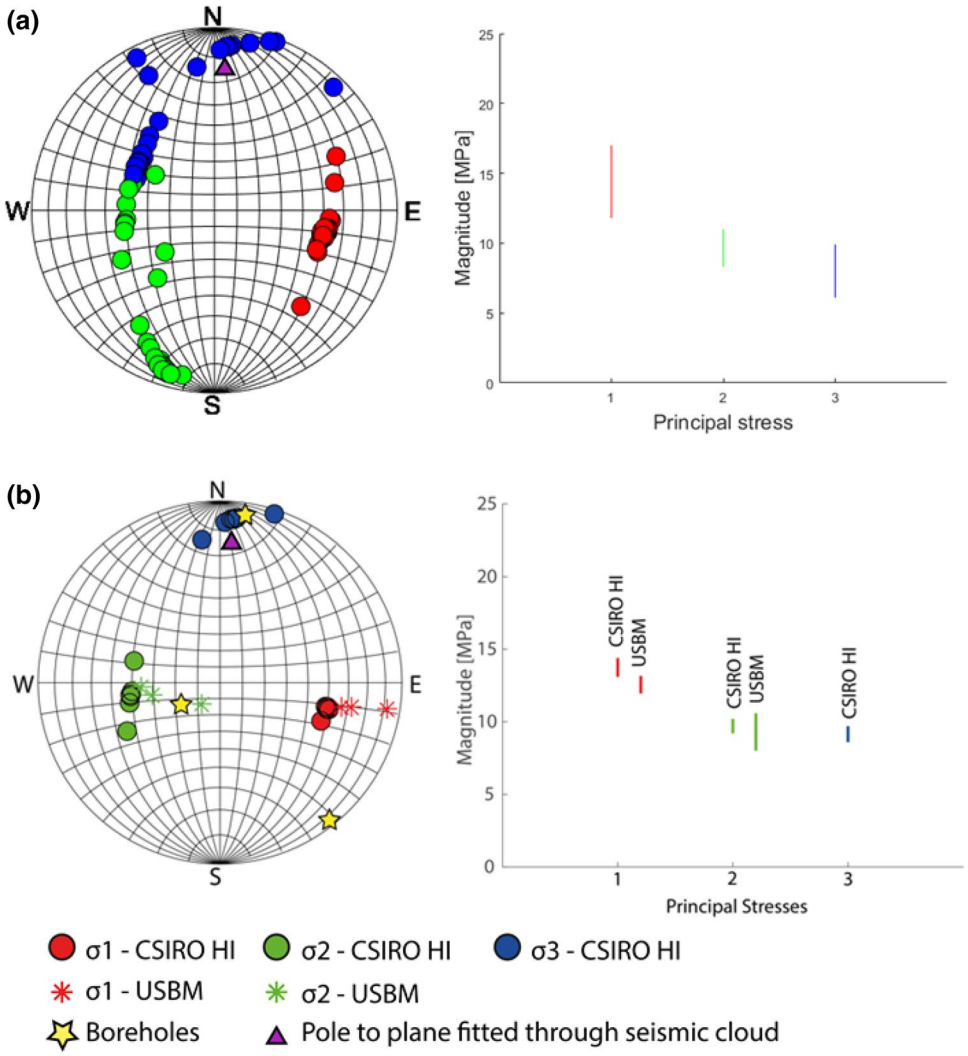

Fig. 11 **a** Stress solutions from the inversion of strains from CSIRO HI test SBH3-2 using the constrained range of transversely isotropic parameters and were further constrained by the minimum stress magnitude of 9.6 MPa from the hydrofracture measurements. **b** Same as in **a** but with the additional constraint that retains only solutions that have a σ_3 orientation that lies within 20° of the pole to the microseismic planes. Additionally, the USBM stress solutions from SBH3 are shown in **b**

in SBH1 scatter around the σ_3 orientation of the unperturbed stress tensor derived from the SBH3 overcoring (actually only CSIRO HI cell). The pole to the plane of microseismicity growth during HF in SBH1 is also plotted, and is clearly also closely aligned with σ_3. Both these observations provide additional support for the view that the unperturbed stress tensor is representative of the stress state prevailing in the relatively unperturbed rock to the south of the test volume.

4.2 Perturbed Stress Field

The SBH4 borehole extends 24 m sub-horizontally from the AU gallery towards N140°E and penetrates an S3 shear zone at 20 m (Fig. 2). Four hydrofracture (HF) measurements conducted along the borehole indicate a progressive reduction in σ_3 from 8.0 MPa at 9.0 m depth to 2.8 MPa at 19.8 m (Fig. 13). Note that the lowest value at 19.8 m, immediately before the shear zone, represents a jacking pressure (i.e., the normal stress on a fracture with unknown orientation) from a multi-cycle step-rate test, and hence σ_3 may be even smaller than 2.9 MPa.

The overcoring results in SBH4 also indicate a trend towards a lower minimum stress level as the S3 shear zone is approached (Fig. 13). A reasonably reliable USBM tests at 8.4 m yielded σ_{min} and σ_{max} values of 7.4 MPa and 9.6 MPa, respectively, and a high-quality measurement at 14.2 m yielded σ_{min} and σ_{max} estimates of 4.8 MPa and 7.5 MPa, respectively. Clearly, at both locations, σ_3 is less than the value of 8.7 MPa that applies to the unperturbed rock to the south of the gallery (Table 8), and significantly so for the deeper measurement. Two successful CSIRO HI cell tests were conducted along SBH4 at 9.2 m (SBH4-2) and at 14.9 m (SBH4-4). The uncertainties in the stress magnitude estimates obtained from the constrained, transverse isotropic elastic inversions shown in Fig. 10c were too large to resolve any trend towards lower σ_3 values with depth along the hole. However, both CSIRO HI cell tests were conducted close to HF tests which yielded σ_3 estimates that are considered reliable. Specifically, a HF test conducted 20 cm from SBH4-2 at 9.2 m yielded a σ_3 estimate of 8.0 MPa, and a test conducted 100 cm from

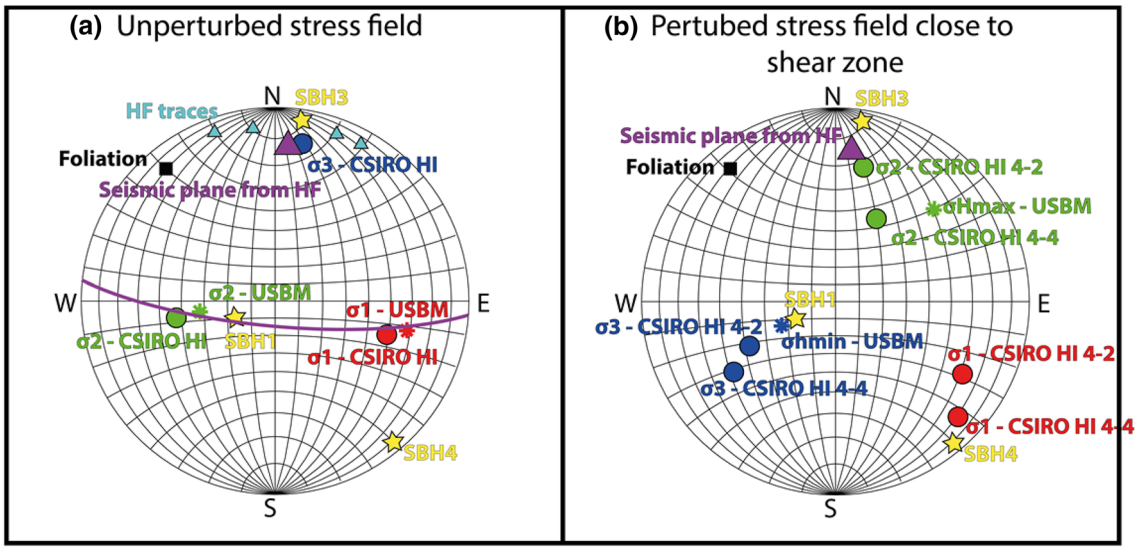

Fig. 12 Final principal stress orientation. **a** Unperturbed principal stress orientations obtained from SBH3 with final tensor represented by CSIRO HI cell measurement combined with averaged USBM results from SBH3. **b** Orientations of the principal stresses obtained close to the shear zone. The CSIRO HI measurements SBH4-2 and −4 represent single solutions based on tensor averaging from the constraint solutions

Table 8 Unperturbed stress tensor derived from the constrained transversely isotropic elastic analysis of the CSIRO HI cell test SBH3-2 further constrained by the upper limit on σ_3 of 9.6 MPa imposed by the hydrofracture tests in SBH1 and SBH3, and by σ_3 orientation within 20° parallel to the pole of the seismic clouds from SBH3

Stress component	Magnitude (MPa)	Dip direction (°)	Dip (°)
σ_1	13.1	104.48	39.21
σ_2	9.2	259.05	47.90
σ_3	8.7	003.72	12.89

SBH4-4 at 14.9 m yielded a σ_3 value of 6.5 MPa. Thus, these HF-derived σ_3 estimates were used to further constrain the stress solutions from the CSIRO HI cell tests by retaining only solutions that were consistent with the HF-derived σ_3 estimates, assuming a 0.5 MPa margin of error. The resulting stress solutions for both SBH4-2 and SBH4-4 are shown in Fig. 14. It should be noted that although the results now indicate a well-resolved trend towards lower σ_3 values with borehole depth, this is a consequence of imposing the additional constraint from the nearby HF tests, rather than an independent result from the CSIRO HI tests alone.

The orientation distributions of the principal stress axes for SBH4-2 and SBH4-4 obtained by imposing the additional HF-derived constraint on σ_3 magnitude shown in Fig. 14 are similar to those in Fig. 10c, except for a reduction in the spread of solutions for each principal axis. It is clear from both figures that the indicated σ_3 orientation for SBH4-2 does not align with the pole to the plane of the microseismic cloud induced

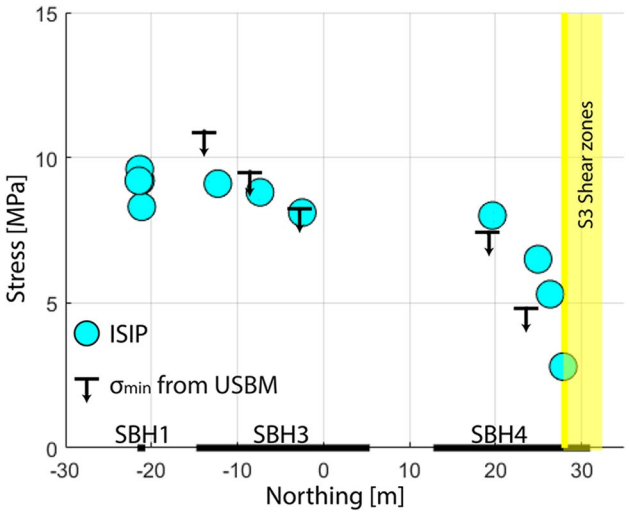

Fig. 13 Variation of ISIPs (i.e., σ_3 estimates) of HFs along a N–S profile together with the upper bounds on σ_3 from the USBM tests. The projections of the three boreholes on the profile is indicated. The figure clearly shows the progressive reduction in σ_3 as the S3-shear zone is approached

during the nearby HF injection (HF4 in Fig. 6) or the sub-planar structures (i.e., clusters) identified within the cloud by (Näf 2017), whose poles are also plotted in Fig. 14. Rather, the poles to the microseismicity planes lie close to the σ_2 orientation. No microseismic planes are plotted in the SBH4-4 stereonets as only 16 locatable events were detected during the adjacent hydrofrac (HF6 in Fig. 6) and they did not define a simple planar structure (Näf 2017). The discrepancy between

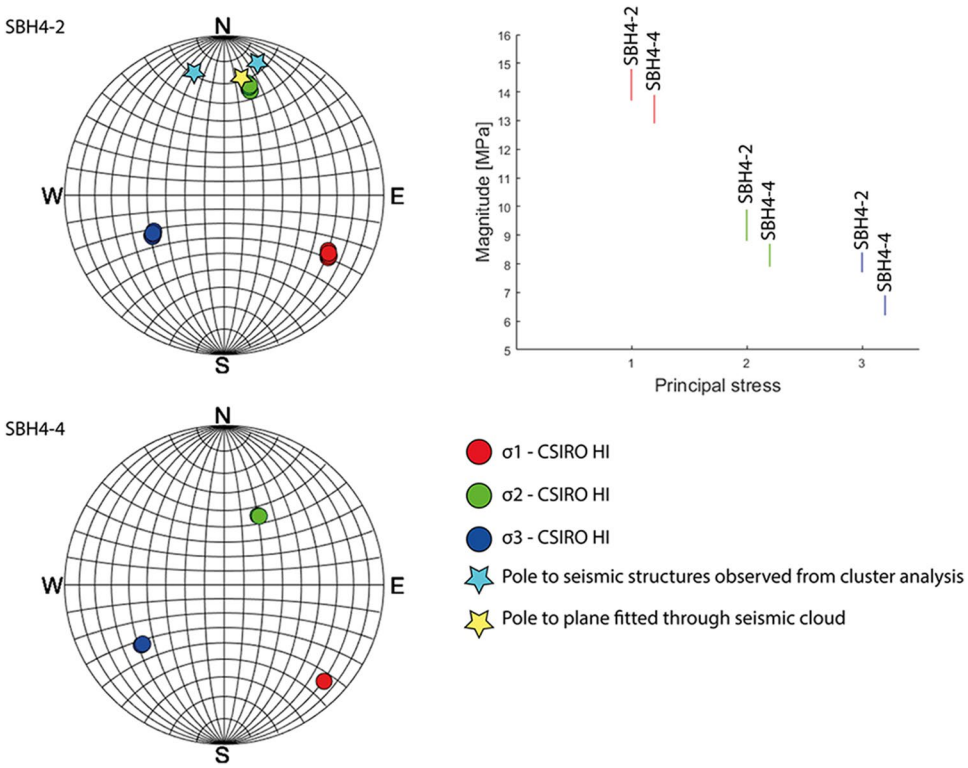

Fig. 14 Stress tensor solutions for SBH4-2 and SBH4-4 after applying the constraint that the σ_3 magnitude lie within 0.5 MPa of the value measured in the neighboring HF test. The orientation of the pole of the best-fit plane to the microseismicity induced during hydrofracture test HF4, whose interval lies 20 cm from SBH4-2, together with those of planar sub-structures (clusters) identified within it are also shown. No plane is shown for SBH4-4 as only 16 locatable events were recorded during the nearest HF test (HF6 in Fig. 6)

the orientation of σ_3 from the SBH4-2 test and the poles to the adjacent induced microseismic structures are best explained as reflecting a degree of structural control in the determining the orientation of the microseismically active planes. As noted earlier, the fracture density in SBH4 is higher than encountered in SBH1 and SBH3 beyond 7 m, and increases with depth, particularly as the S3 shear zone is approached. This perhaps explains why the microseismic clouds induced during the HF tests had a more diffusive character than those in SBH3, which were more compact and planar. Furthermore, as is clear from Fig. 14, the difference between the magnitudes of σ_3 and σ_2 near SBH4-2 is only of the order of 1 MPa. Such small differences promote structural involvement in determining the failure process and the pattern of microseismicity that accompanies it. In any case, the collective data from SBH4 indicates that it penetrates a rock mass where the stress state becomes progressively more perturbed, and strongly so as the S3 shear zone is approached. Thus, the best-fitting stress tensors for SBH4-2 and SBH4-2 derived by tensor averaging of the solutions in Fig. 14, are shown in the 'perturbed' frame in Fig. 12.

5 Discussion

5.1 Method Integration

The approach to characterize stresses within and about the test volume involved overcoring, hydraulic fracturing/ HTPF and monitoring of the pattern of microseismicity induced by the HF injections. The use of different methods proved crucial for the correct interpretation of the data. In particular, it revealed the importance of using a correctly parametrized, transversely isotropic rock model for inverting the overcoring strain data. It was already known that anisotropy can have great influence on stress inversions (Amadei 1996), and that rock with bedding planes or a distinct foliation commonly displays transversely isotropic elastic behavior (Bjarnason et al. 1988; Ask 2003; Christiansson and Janson 2003). Interpretation of the CSIRO HI cell strain data with isotropic elastic rock models parametrized by in situ pressure-cell tests led to stress estimates that were inconsistent with the HF and microseismic data. Only by adopting a transversely isotropic model parametrized by a procedure that involved numerical modelling of the in situ pressure-cell data supplemented by laboratory tests on core plugs could the discrepancies between the various types of data be reconciled.

5.2 Comparison with Pre-existing Stress Measurements

Previous stress determinations in the Grimsel region show a considerable scatter in the orientation of σ_1, with azimuths ranging from N40°E to N160°E. In the GTS, the most complete stress measurements were a series of predominantly overcoring tests performed by Pahl et al. (1989) in the 191 m deep vertical hole in the BK cavern, located 300 m north of the ISC site. Taken on face value, the results show considerable

variations in stress magnitude and orientation, with a large change occurring across a significant shear zone with open fractures at 100 m depth in the hole. Above this feature, σ_1 had a wide range of orientations and thrust faulting was favored, whereas below this zone, the stress state was strike slip with σ_1 oriented approximately E–W. Thus, stress changes associated with shear structures had already been observed at the GTS before the present measurements revealed the change associated with the S3 shear zone at the ISC site.

The σ_1 orientation in the unperturbed rock at the ISC site in the GTS has an E–W orientation, consistent with the stress orientation below the shear zone in the BK borehole. An E–W orientation for σ_1 was also obtained with deep hydrofracture measurements to 560 m depth in the Kessiturm borehole, 2 km to the south of the GTS (Bühler 2011), and with the hydrofracture measurements to 80 m depth in the Handeck borehole, some 4 km to the north of the GTS (Rummel and Klee 2009). Thus, the balance of evidence favors an E–W orientation for σ_1 in the Grimsel area, although the observations at the ISC and BK sites in the GTS clearly show there are local deviations from this direction.

The unperturbed stress state at the ISC site in the GTS is strike slip with σ_3 oriented N–S and σ_2 sub-vertical. This is consistent with the stress state below the shear zone at 100 m depth in the BK borehole, although the stress state above this zone, which is at the same level as the ISC site, favors reverse faulting. A stress state favoring reverse faulting was also found at the Kessiturm and Handeck boreholes. It is likely that the severe topography in the Grimsel region would give rise to local variations in stress state, although in the GTS it is clear that changes in stress state can occur across shear zones.

5.3 Stress Heterogeneities

The stress characterization indicates that the stress state in the rock mass penetrated by the SBH1 and SBH3 boreholes in the south of the ISC study volume is reasonably uniform. In contrast, a marked drop in minimum stress magnitude and a change in orientation occurs along the SBH4 borehole as the S3 shear zone is approached. The existence of this stress change is potentially important for understanding the data obtained from the ISC experiment, and so it was explicitly acknowledged in the stress characterization by defining a perturbed stress zone in the vicinity of the S3 shear zone. For this reason, only the data collected in the SBH1 and SBH3 boreholes were averaged to obtain a stress tensor that is considered to represent the unperturbed stress state.

Variations in stress near fractures and shear zones have been reported by several authors (Bell et al. 1992; Davatzes and Hickman 2005; Valley and Evans 2010). In the present case, the nature of the implied stress heterogeneity is uncertain, although two mechanisms that could potentially contribute are suggested. First, the magnitude change along SBH4 correlates with an increase in the degree of fragmentation observed from borehole and core logs that includes open fractures and a zone of low P-wave velocity that extends between two distinct S3 shear structures at the margins of metabasic dykes, as inferred from seismic tomography (Fig. 2). The higher degree of fragmentation within and near the S3 zone would render the rock more compliant compared to the surrounding less perturbed rock, so it could act as an elastic inclusion and perturb the stress field in the vicinity (Eshelby 1957; Casey 1980; Faulkner et al. 2006). Note that the low velocity zone appears to be limited to the eastern part of the shear zones. If the associated zone of lower stiffness is similarly localized, then changes in stress along the S3 structure would be expected. A second mechanism that might contribute to the observed decrease in σ_3 near the S3 shear zone is the stress perturbation arising from slip along the fractures within the zone (Shamir and Zoback 1992; Valley and Evans 2010). The results of a slip tendency analysis of the S3 shear zone under both the unperturbed and perturbed stress tensors shown in Fig. 12 is presented in Fig. 15. A friction coefficient of 0.8 was assumed. A Mohr–Coulomb failure criterion was applied that neglected the intermediate principal stress. This approach seemed reasonable, as σ_2 and σ_3 are similar in magnitude. The results indicate that the S3 shear zone is not critically stressed under both stress tensors, as a pore pressure of at least 5 MPa would be required to initiate failure. Thus, any slip-related stress perturbation that is present must be an artifact of slip in the past as the feature is not currently active.

6 Conclusions

The availability of data from different measurement techniques proved crucial for the successful characterization of the stress state within the metamorphic foliated granite of the decameter scale ISC test volume at the Grimsel Test Site. By combining data from six successful USBM and three CSIRO HI cell overcoring tests, nine hydraulic fracturing tests, and detailed mapping of the microseismicity induced during the HF tests, it was shown that the stress state in the relatively unfractured rock mass in the southern part of the test volume was reasonably uniform, whereas a progressive drop in minimum principal stress and a change in stress orientation was observed near a shear zone that cuts the test volume to the NNW. Consistency between the CSIRO HI cell stress solutions and the hydrofracture and microseismicity observations could only be obtained using a transversely isotropic rock model for the stress inversion of the overcoring data. The model was parametrized by numerical modelling of the in situ pressure test data, supplemented by laboratory tests. Both uniaxial compression laboratory tests and a sensitivity

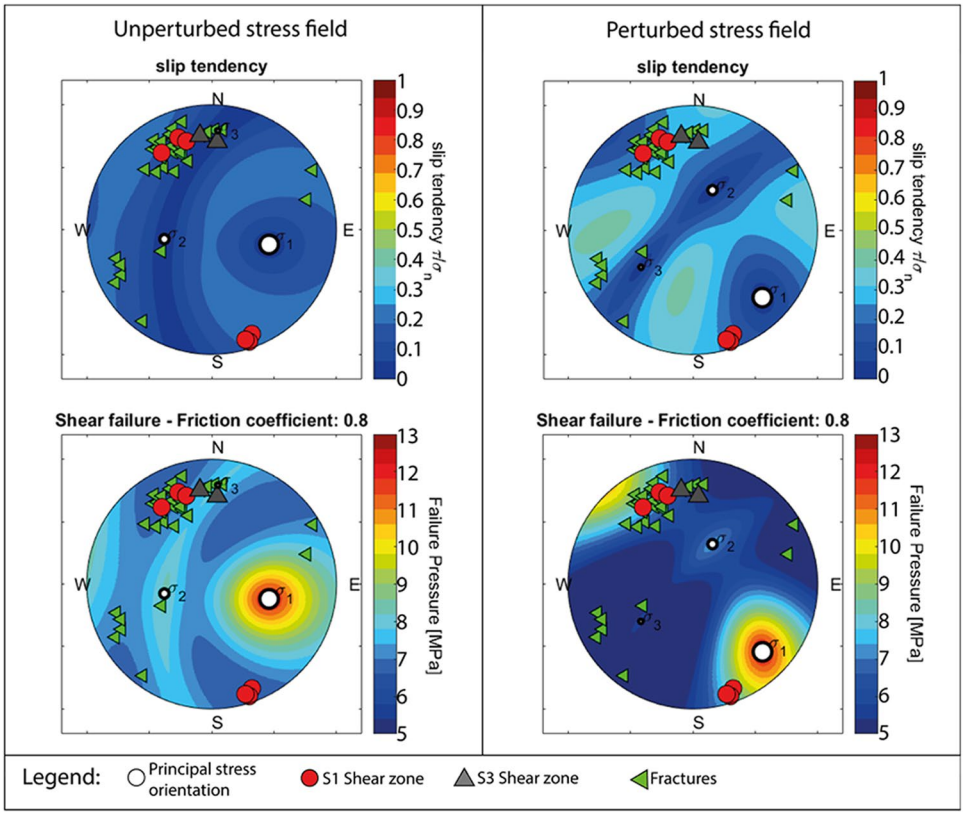

Fig. 15 Slip tendencies and shear failure for unperturbed and perturbed stress tensors. The failure pore pressure was calculated based on a friction coefficient of 0.8

analysis for the stress inversion indicated the factor of anisotropy (E_2/E_1) for the foliated granite was approximately 0.5.

The stress tensor obtained for the southern part of the test volume, referred to as the unperturbed stress state, has principal stress magnitudes that range between 13.1 and 14.4 MPa for σ_1, 9.2 and 10.2 MPa for σ_2, and 8.6 and 9.7 MPa for σ_3. The orientation of σ_1 plunges to the east at an angle of 30–40°. Although σ_2 and σ_3 have a similar magnitude within their ranges of uncertainty, the planar nature and similar orientation (i.e., sub-vertical striking EW) of all microseismic clouds induced by hydrofracturing tests in the southern part of the test volume suggests that σ_3 is decidedly less than σ_2 and is oriented NS and sub-horizontal.

The stress variation in the NNW part of the test zone is defined by a progressive reduction of minimum principal stress measured along a 24 m long sub-horizontal borehole drilled through a shear zone towards the NNW. Specifically, the value of σ_3 drops from 8.6 to ~3 MPa as the shear zone is approached. Changes in stress at shear zones were evident in earlier stress measurements campaigns at the GTS. In the present case, the extent and origin of the disturbance is uncertain, although two mechanisms that could contribute are suggested by the observations. First, borehole logs, core inspection and seismic tomography indicate the stress change coincides with more fragmented and thus elastically compliant rock, which could behave as an inclusion and locally disturb the stresses. Second, the brittle slip recorded in the shear zone would give rise to a stress perturbation. A slip tendency analysis indicates it is not currently critically stressed, and so such slip must have occurred some time ago when the stress was different.

Acknowledgements The ISC is a project of the Deep Underground Laboratory at ETH Zurich, established by the Swiss Competence Center for Energy Research—Supply of Electricity (SCCER-SoE) with the support of the Swiss Commission for Technology and Innovation (CTI). Funding for the ISC project was provided by the ETH Foundation with grants from Shell, EWZ, and by the Swiss Federal Office of Energy through a P&D grant. Hannes Krietsch is supported by SNF grant 200021_169178. The Grimsel Test Site is operated by Nagra, the National Cooperative for the Disposal of Radioactive Waste. We are indebted to Nagra for hosting the ISC experiment in their GTS facility and to the Nagra technical staff for on-site support. Additionally, we like to thank INERIS and Solexperts (MeSY) for conducting the field acquisition of overcoring tests, and HF tests, respectively. Last but not least, we like to thank Rico Näf, who analyzed the seismic data recorded during HF in SBH4.

Appendix

See Figs. 16, 17, 18, 19, 20 and 21.

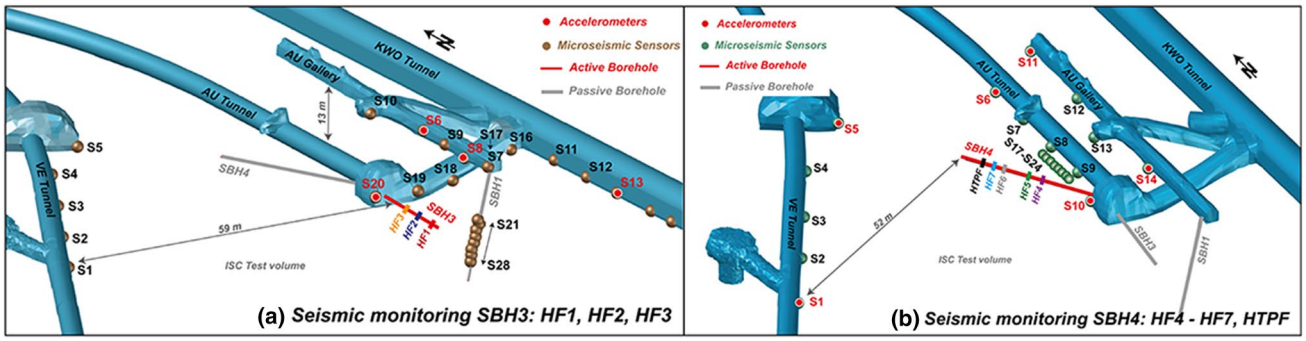

Fig. 16 Seismic monitoring network during hydraulic fracturing in SBH3 (**a**) and SBH4 (**b**), modified after Jalali et al. (2018)

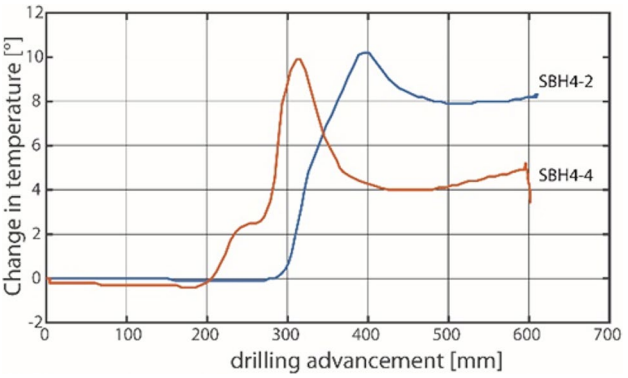

Fig. 17 Increase in temperature during drilling advancement in SBH4 CSIRO HI overcoring

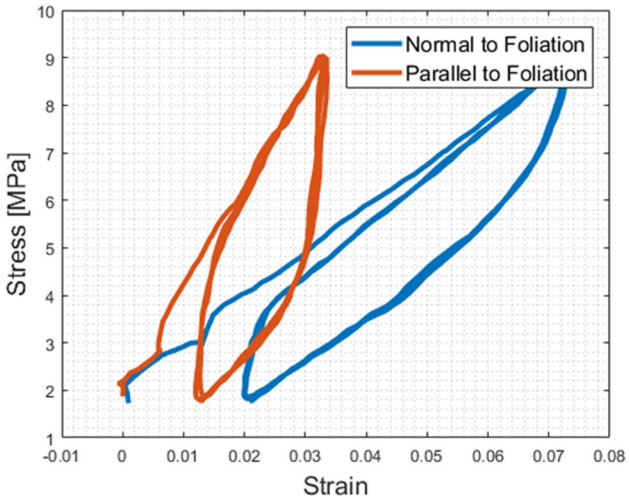

Fig. 18 Stress–strain curve from uniaxial tests of ISC core plugs. Samples were tested in two orientations: **a** normal to foliation (blue), **b** parallel to foliation (red). (Color figure online)

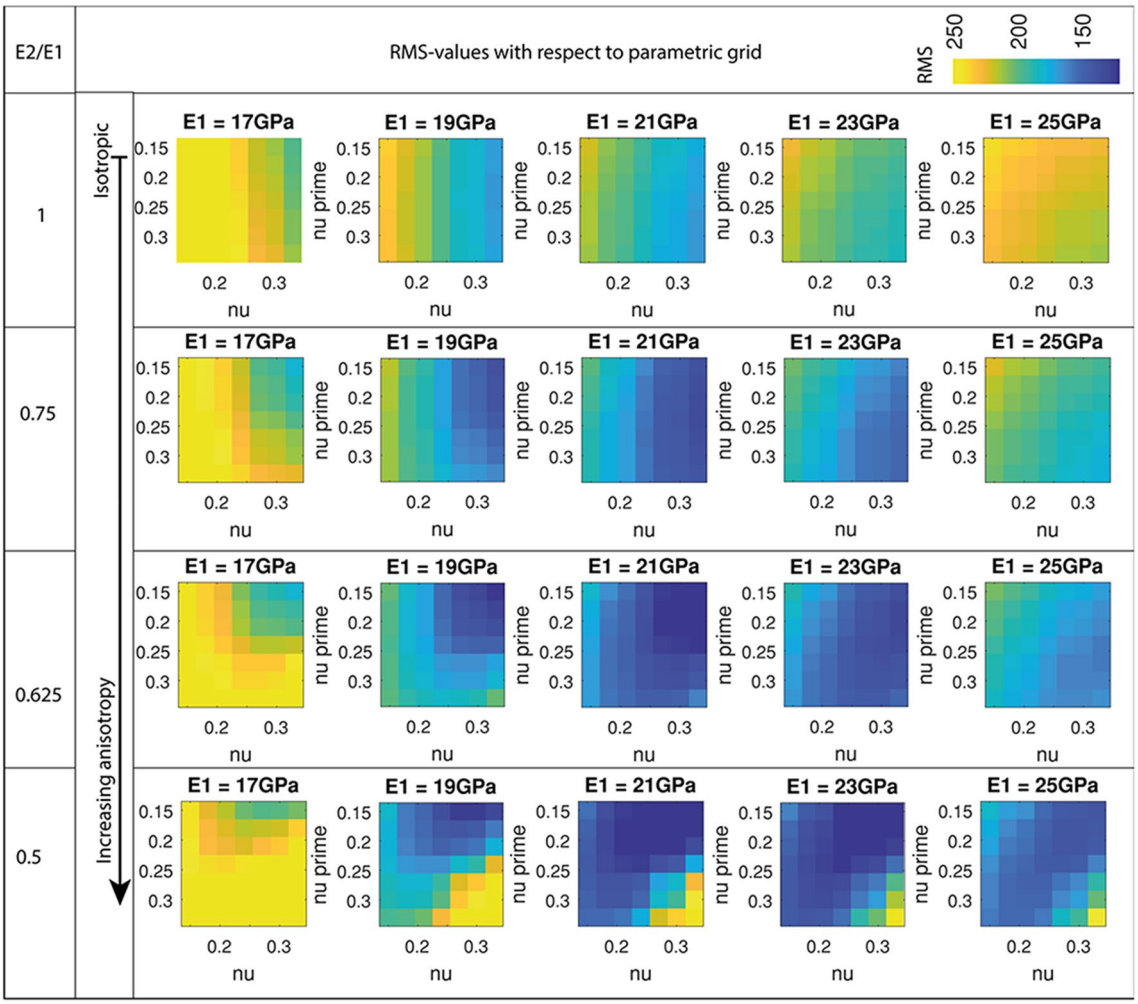

Fig. 19 RMS evaluation for parametric grid used in the biaxial test simulator for SBH3-2

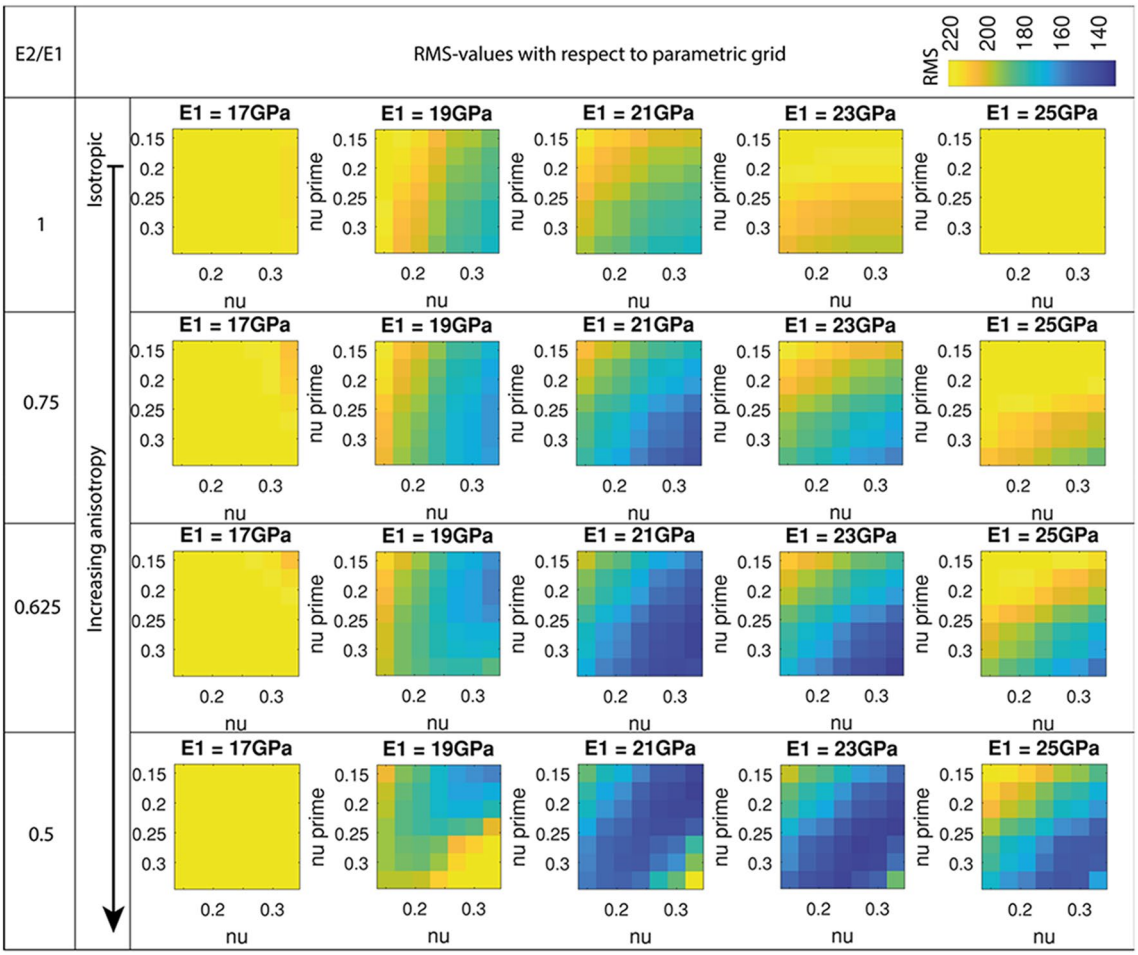

Fig. 20 RMS evaluation for parametric grid used in the biaxial test simulator for SBH4-2

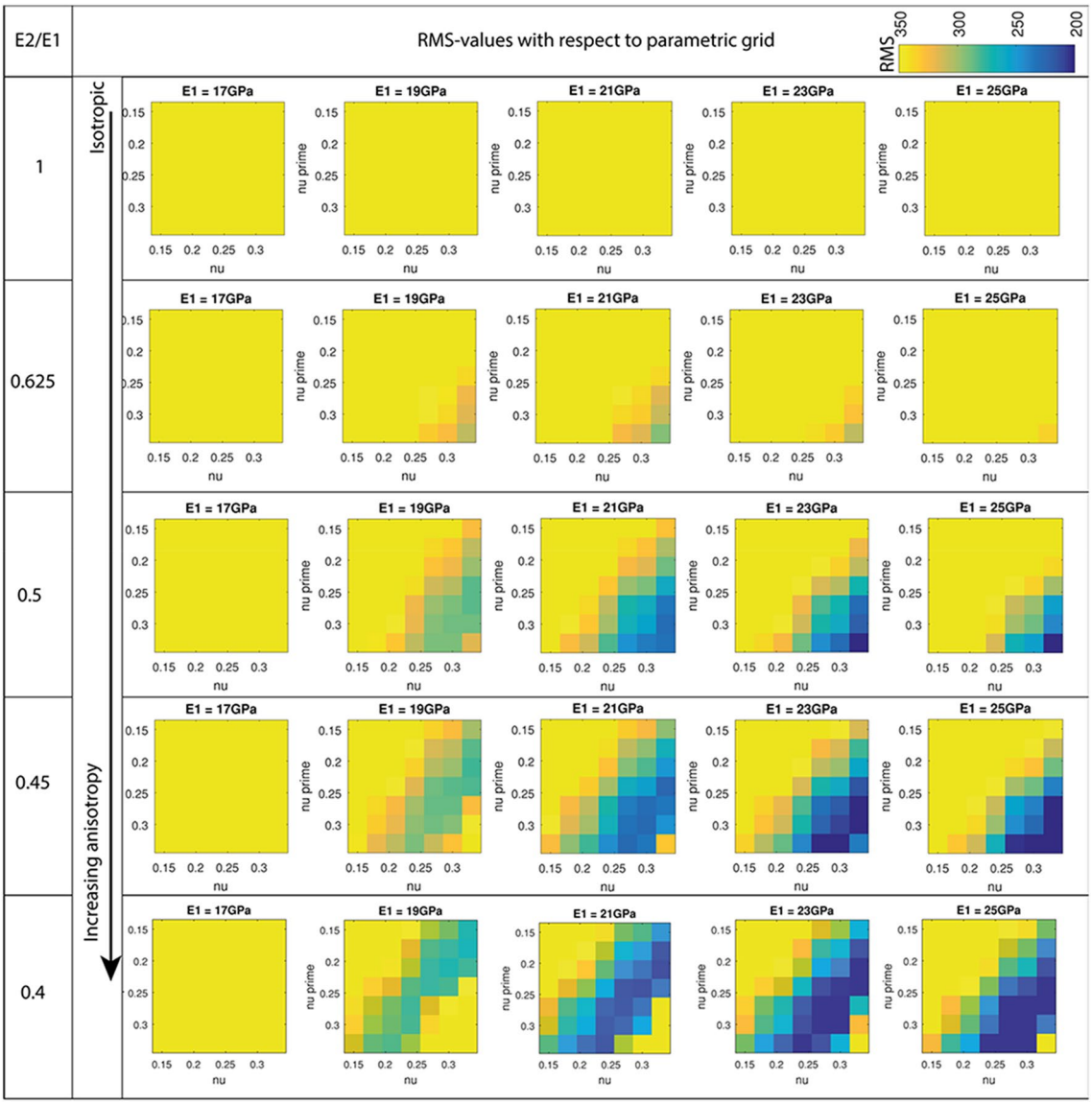

Fig. 21 RMS evaluation for parametric grid used in the biaxial test simulator for SBH4-4

References

Amadei B (1996) Importance of anisotropy when estimating and measuring in situ stresses in rock. Int J Rock Mech Min Sci Geomech Abstr 33:293–325. https://doi.org/10.1016/0148-9062(95)00062-3

Amadei B (2000) CSIRA: a computer program to determine in situ stresses by overcoring in anisotropic rock with CSIR-type triaxial strain cells. University of Colorado, Boulder

Amadei B, Stephansson O (1997) Rock stress and its measurement, 9th edn. Chapman&Hall, London

Amann F, Gischig V, Evans KF et al (2018) The seismo-hydromechanical behavior during deep geothermal reservoir stimulations: open questions tackled in a decameter-scale in situ stimulation experiment. Solid Earth 9:115–137. https://doi.org/10.5194/se-9-115-2018

Ask D (2003) Evaluation of measurement-related uncertainties in the analysis of overcoring rock stress data from Äspö HRL, Sweden: a case study. Int J Rock Mech Min Sci 40:1173–1187. https://doi.org/10.1016/S1365-1609(03)00114-X

Ask D (2006a) New developments in the integrated stress determination method and their application to rock stress data at the Äspö HRL, Sweden. Int J Rock Mech Min Sci 43:107–126. https://doi.org/10.1016/j.ijrmms.2005.04.011

Ask D (2006b) Measurement-related uncertainties in overcoring data at the Äspö HRL, Sweden. Part 2: biaxial tests of CSIRO HI overcore samples. Int J Rock Mech Min Sci 43:127–138. https://doi.org/10.1016/j.ijrmms.2005.05.012

Barton CA, Zoback MD (1994) Stress perturbations associated with active faults penetrated by boreholes: possible evidence for near-complete stress drop and a new technique for stress magnitude

measurement. JGR Solid Earth 99:9379–9390. https://doi.org/10.1029/93JB03359
Bell JS, Caillet G, Adams J (1992) Attempts to detect open fractures and non-sealing faults with dipmeter logs. Geol Soc Lond Spec Publ 65:211–220. https://doi.org/10.1144/GSL.SP.1992.065.01.16
Bjarnason B, Leijon B, Stephansson O (1988) The Bolmen project: rock stress measurements using hydraulic fracturing and overcoring techniques. Tunn Undergr Space Technol 3:305–316. https://doi.org/10.1016/0886-7798(88)90058-2
Bouffier C (2015) Stress measurements by overcoring at the Grimsel site—results from the campaign of August–September 2015. INERIS, Nancy
Bühler C (2011) Kraftwerke Oberhasli—Spannungsmessungen mit hydraulic fracturing in Bohrung GRI3. Stump, Polymetra
Casey M (1980) Mechanics of shear zones in isotropic dilatant materials. J Struct Geol 2:143–147. https://doi.org/10.1016/0191-8141(80)90044-9
Challandes N, Marquer D, Villa IM (2008) P-T-t modelling, fluid circulation, and ^{39}Ar–^{40}Ar and Rb-Sr mica ages in the Aar Massif shear zones (Swiss Alps). Swiss J Geosci 101:269–288. https://doi.org/10.1007/s00015-008-1260-6
Christiansson R, Janson T (2003) A test of different stress measurement methods in two orthogonal bore holes in Äspö Hard Rock Laboratory (HRL), Sweden. Int J Rock Mech Min Sci 40:1161–1172. https://doi.org/10.1016/j.ijrmms.2003.07.006
Cornet FH (1993) The HTPF and the integrated stress determination methods. In: Rock testing and site characterization. Pergamon, Oxford, pp 413–432
Davatzes NC, Hickman S (2005) Comparison of acoustic and electrical image logs from the Coso geothermal field, CA. In: Thirtieth Workshop on Geothermal Reservoir Engineering. Stanford University, Stanford
Doetsch J, Krietsch H, Lajaunie M et al. (2017) Characterizing fractures and shear zones in crystalline rock using anisotropic seismic inversion and GPR imaging. In: EGU General Assembly ConferenceAbstracts, vol 19, p 15518
Eshelby JD (1957) The determination of the elastic field of an ellipsoidal inclusion, and related problems. Proc R Soc Lond A 241:376–396. https://doi.org/10.1098/rspa.1957.0133
Evans KF, Oertel G, Engelder T (1989) Appalachian Stress Study: 2. Analysis of Devonian shale core: some implications for the nature of contemporary stress variations and Alleghanian deformation in Devonian rocks. JGR Solid Earth 94:7155–7170
Faulkner DR, Mitchell TM, Healy D, Heap MJ (2006) Slip on "weak" faults by the rotation of regional stress in the fracture damage zone. Nature 444:922–925. https://doi.org/10.1038/nature05353
Gischig V, Doetsch J, Maurer H et al (2018) On the link between stress field and small-scale hydraulic fracture growth in anisotropic rock derived from microseismicity. Solid Earth 9:39–61. https://doi.org/10.3929/ethz-b-000238888
Gruner U, Ziegler H (2011) Pumpspeicherwerk Grimsel 3. Sondierbohrung Kessiturm. Kellerhals&Haefeli AG, Bern
Guglielmi Y, Cappa F, Avouac J-P et al (2015) Seismicity triggered by fluid injection–induced aseismic slip. Science 348:1224–1226. https://doi.org/10.1126/science.aab0476
Haimson BC, Cornet FH (2003) ISRM suggested methods for rock stress estimation—Part 3: hydraulic fracturing (HF) and/or hydraulic testing of pre-existing fractures (HTPF). Int J Rock Mech Min Sci 40:1011–1020. https://doi.org/10.1016/j.ijrmms.2003.08.002
Hooker VE, Bickel DL (1974) Overcoring equipment and techniques: used in rock stress determination. US Bureau of Mines, Washington, D.C.
Hubbert M, Willis DG (1957) Measurement of hydraulic fracturing
Jalali M, Gischig V, Doetsch J et al (2018) Transmissivity changes and microseismicity induced by small-scale hydraulic fracturing tests in crystalline rock. Geophys Res Lett 45:2265–2273. https://doi.org/10.1002/2017GL076781
Keusen HR, Ganguin J, Schuler P, Buletti M (1989) Felslabor Grimsel Geologie Nagra Technischer Bericht NTB 87–14. NAGRA & GEOTEST, Zollikofen//Bern
Klee G (2015) Hydraulic-fracturing and HTPF Tests in Borehole NOS SB15.001, SB15.003 and SB15.004. MeSy Solexperts
Konietzky H, Marshall P (1997) Excavations disturbed zone around tunnels in fractured rock—example from the Grimsel Test Site. Geomechanics 96:235–240
Krietsch H, Gischig V, Jalali MR et al (2017) Stress measurements in crystalline rock: comparison of overcoring, hydraulic fracturing and induced seismicity results. American Rock Mechanics Association, Alexandria
Leijon BA (1989) Relevance of pointwise rock stress measurements—an analysis of overcoring data. Int J Rock Mech Min Sci Geomech Abstr 26:61–68. https://doi.org/10.1016/0148-9062(89)90526-3
Näf R (2017) Microseismic monitoring of hydrofractures in crystalline rock
Pahl A, Heusermann S, Bräuer V, Göggler W (1989) Grimsel test site—rock stress investigations. Federal Institute for Geosciences and Natural Resoureces, Hannover
Rummel F, Klee G (2009) Durchfürhung von Hydraulik- und Hydrofrac-Spannungsmessungen der Bohrung Handegg-1. Solexperts AG, Mönchaltorf
Saint-Venant B (1863) Sur la distribution des élasticités autour de chaque point d'un solide ou d'un milieu de contexture quelconque, particulièrement lorsqu'il est amorphe sans être isotrope. J Math Pures Appl 8:257–430
Schneeberger R, de La Varga M, Egli D et al (2017) Methods and uncertainty estimations of 3-D structural modelling in crystalline rocks: a case study. Solid Earth 8:987–1002. https://doi.org/10.5194/se-8-987-2017
Shamir G, Zoback M (1992) Stress orientation profile to 3.5 km depth near the San Andreas Fault at Cajon Pass, California. JGR Solid Earth 97:5059–5080
Sjöberg J, Christiansson R, Hudson JA (2003) ISRM Suggested Methods for rock stress estimation—Part 2: overcoring methods. Int J Rock Mech Min Sci 7–8:999–1010. https://doi.org/10.1016/j.ijrmms.2003.07.012
Steck A (1968) Die alpidischen Strukturen in den Zentralen Aaregraniten des westlichen Aarmassivs. Eclogae Geol Helvetiae 61:19–48. https://doi.org/10.5169/seals-163584
Stephansson O, Zang A (2015) The ISRM suggested methods for rock characterization, testing and monitoring: 2007–2014. Rock Mech Rock Eng. https://doi.org/10.1007/978-3-319-07713-0
Valley B, Evans KF (2009) Stress orientation to 5 km depth in the basement below Basel (Switzerland) from borehole failure analysis. Swiss J Geosci 102:467. https://doi.org/10.1007/s00015-009-1335-z
Valley B, Evans KF (2010) Stress heterogeneity in the Granite of the Soultz EGS reservoir inferred from analysis of Wellbore failure. In: Proceedings world geothermal congress. Bali, p 13
Wehrens P, Baumberger R, Berger A, Herwegh M (2017) How is strain localized in a meta-granitoid, mid-crustal basement section? Spatial distribution of deformation in the central Aar massif (Switzerland). J Struct Geol 94:47–67. https://doi.org/10.1016/j.jsg.2016.11.004
Wileveau Y, Cornet FH, Desroches J, Blumling P (2007) Complete in situ stress determination in an argillite sedimentary formation. Phys Chem Earth Parts ABC 32:866–878. https://doi.org/10.1016/j.pce.2006.03.018

Wohnlich M (1999) In-situ stress measurements (post-excavation) in the boreholes GMT 98-001/GMT 98-003 and GMT 99-006. NAGRA, Wettingen

Worotnicki G (1993) CSIRO triaxial stress measurement cell. In: Comprehensive rock engineering. 3rd edn, pp 329–394

Worotnicki G, Walton RJ (1976) CSIRO Research Publications Repository—Triaxial "hollow inclusion" gauges for determination of rock stress in situ. Institution of Engineers, Sydney

Yaméogo ST, Corthésy R, Leite MH (2013) Influence of rock failure and damage on in situ stress measurements in brittle rock. Int J Rock Mech Min Sci 61:118–129. https://doi.org/10.1016/j.ijrmms.2013.02.011

Zang A, Lienert M, Zinke J, Berckhemer H (1996) Residual strain, wave speed and crack analysis of crystalline cores from the KTB-VB well. Tectonophysics 263:219–234. https://doi.org/10.1016/S0040-1951(96)00033-9

Zang A, Stephansson O, Stenberg L et al (2017) Hydraulic fracture monitoring in hard rock at 410 m depth with an advanced fluid-injection protocol and extensive sensor array. Geophys J Int 790–813